



저작자표시-비영리-변경금지 2.0 대한민국

이용자는 아래의 조건을 따르는 경우에 한하여 자유롭게

- 이 저작물을 복제, 배포, 전송, 전시, 공연 및 방송할 수 있습니다.

다음과 같은 조건을 따라야 합니다:



저작자표시. 귀하는 원저작자를 표시하여야 합니다.



비영리. 귀하는 이 저작물을 영리 목적으로 이용할 수 없습니다.



변경금지. 귀하는 이 저작물을 개작, 변형 또는 가공할 수 없습니다.

- 귀하는, 이 저작물의 재이용이나 배포의 경우, 이 저작물에 적용된 이용허락조건을 명확하게 나타내어야 합니다.
- 저작권자로부터 별도의 허가를 받으면 이러한 조건들은 적용되지 않습니다.

저작권법에 따른 이용자의 권리는 위의 내용에 의하여 영향을 받지 않습니다.

이것은 [이용허락규약\(Legal Code\)](#)을 이해하기 쉽게 요약한 것입니다.

[Disclaimer](#)

Ph.D. DISSERTATION

Vibration-based Structural Health
Monitoring using Machine Learning
with Applications to Plate and Pipeline
Structures

기계 학습을 이용한 진동 기반 구조물 건전성
모니터링 기법의 판과 파이프 구조물에의 응용

BY

Sunah Jung

AUGUST 2019

DEPARTMENT OF NAVAL ARCHITECTURE AND
OCEAN ENGINEERING
COLLEGE OF ENGINEERING
SEOUL NATIONAL UNIVERSITY

Abstract

Structural health monitoring (SHM) is essential to large structures for safety and economic benefits. In order to monitor the condition of structures, statistical analysis using machine learning algorithms has been used in recent years. Conventional vibration-based monitoring approaches generally utilize modal parameters of mode frequency, modal damping, or mode shape. The issue is that damages are generated locally and may not considerably influence the modal parameters, especially under ambient vibrations. Recent works on ambient noise interferometry have shown that the noise cross-correlation of diffuse fields can be useful for SHM application. Based on this recent signal processing method, the vibration-based SHM using diffuse fields is developed in this dissertation. A laboratory experiment is investigated on an aluminum plate with two accelerometers. A hand-held impact hammer is operated for the excitation and two types of damages are examined. From the cross-correlation of diffuse fields between two receivers, damage-sensitive statistical features are extracted. The performance is analyzed according to various environmental conditions and damage types applying a novel damage detection algorithm, support vector machine (SVM). Meanwhile, in flow monitoring of a pipeline-riser system, early recognition of severe slugging is important to prevent negative impacts including structural damage and low production. In this dissertation, a new monitoring approach using vibration signals of accelerometers is suggested. A main characteristic of accelerometer that vibration signals are significantly different between stable flow and unstable flow is advantageous for early recognition of severe slugging. An experimental study is performed in the pipeline-riser system, where six accelerometers are installed from

the bottom to the top of the vertical riser. Different environmental conditions are generated by changing water and gas superficial velocities. Simple statistical parameters and linear prediction coefficients are extracted from vibration data for online recognition. The SVM and neural network (NN) are applied for binary classification, and the NN is used for multiclass classification. The performance is evaluated according to the signal length with different sensor locations. Though this dissertation is focused on the damage detection in the plate structure and unstable flow monitoring of the pipeline-riser system, the suggested methods can be useful with appropriate feature extraction for many SHM problems, such as blockage detection in the pipeline, condition monitoring of ship structures, and monitoring of building structures.

Keyword: Structural health monitoring, Cross correlation, Ambient vibration, Severe slugging, Pipeline-riser structure, Machine learning

Student Number: 2015-31036

Table of Contents

Abstract	i
Table of Contents	iii
List of Figures	v
1 Introduction.....	1
1.1. Structural health monitoring	1
1.2. Damage detection on the aluminum plate.....	2
1.3. Severe slugging detection in the pipeline-riser system	6
1.4. Organization of the Dissertation	8
2 Machine learning algorithms for structural health monitoring....	14
2.1. Principal component analysis (PCA)	15
2.2. Support vector machine (SVM)	17
2.3. Neural network (NN)	24
3 Damage detection on the aluminum plate	28
3.1. Introduction.....	29
3.2. Theoretical background.....	31
3.3. Experiment and data processing	36
3.4. Damage detection.....	44
3.5. Summary and conclusions	60
3.6. Acknowledgement.....	61
4 Severe slugging detection in the pipeline-riser system	67
4.1. Introduction.....	68
4.2. Theoretical background.....	71
4.3. Experimental apparatus and procedure	78

4.4. Classification method.....	88
4.5. Classification results and discussion.....	94
4.6. Summary and conclusions	100
4.7. Acknowledgments.....	102
5 Summary	108
Appendix	111
A.1. Classification without PCA in damage detection on the plate	111
A.2. Optimized parameters in severe slugging detection.....	113
A.3. Classification with additional features of frequency domain signals..	116
Abstract (In Korean).....	117

List of Figures

Figure 1-1: Outline of damage detection in the plate structure.....5

Figure 1-2: Outline of unstable flow monitoring in the pipeline-riser system...8

Figure 2-1: Samples of multivariate Gaussian distribution centered at $(0, 0)$ with a covariance matrix $\begin{bmatrix} 1 & 1.5 \\ 1.5 & 3 \end{bmatrix}$15

Figure 2-2: Example of data distribution composed of two-classes. Data of $t_n = +1$ are presented as square markers and have $y(\mathbf{x}_n) > 0$. And data of $t_n = -1$ are described as circle markers and have $y(\mathbf{x}_n) < 0$. The margin is the distance between the hyperplane of green solid line and a red circle marker of $t_n = -1$19

Figure 2-3: Example of data distribution composed of two-classes with misclassified samples. Data of $t_n = +1$ are presented as square markers, and data of $t_n = -1$ are described as circle markers. Misclassified sample of circle marker with red dashed line has $\xi_n > 1$21

Figure 2-4: Structure of basic feedforward NN. It has D inputs, M units of hidden layer, and K outputs.25

Figure 3-1: Extraction of the noise cross-correlation function (NCF) from ambient vibrations. Separate N noise sources are used, denoted as circled text 1, 2, ... N to produce the diffuse field.33

Figure 3-2: Experimental setup. Aluminum plate is 40 cm in width and length with a 2 mm-thickness. Two accelerometers are placed at $(x, y) = (27 \text{ cm}, 13 \text{ cm})$ and $(13 \text{ cm}, 27 \text{ cm})$ and damages are at the center of the plate....37

Figure 3-3: Histogram of a thousand zero-delay cross-correlation coefficient38

Figure 3-4: Typical spectrum of an impulse hammer excitation. The black solid line presents the spectrum from the impulse hammer and the blue dotted line is the noise spectrum in case of no excitation. Most of the impulse energy is distributed below 7 kHz.39

Figure 3-5: Experimental configuration.....40

- Figure 3-6: (a) NCF for 118 excitations of the undamaged plate. The averaged NCF is symmetric in time for fully diffuse field. The zero-delay cross-correlation coefficient of the left and right parts of the averaged NCF is 0.994. (b) Blow up of (a) for [-0.05 0.05].42
- Figure 3-7: Zero-delay cross-correlation coefficients between the averaged NCFs of N and 118 excitations as a function of N. The N sources are randomly chosen among a total of 118 sources. A total of one hundred trials are conducted in (a) and larger fluctuations are shown in the small number of sources. (b) Mean curve of coefficients according to N.....43
- Figure 3-8: Mean of each damage index distribution. (a) Mean, (b) variance, (c) skewness, (d) kurtosis, (e) RMS according to N.45
- Figure 3-9: (a) The normalized NCF defined as $f(t) = \frac{(\langle C_{12}(t) \rangle_{118})^2}{\int_0^\infty (\langle C_{12}(t) \rangle_{118})^2 dt}$, (b) the CDF of $f(t)$. The black solid line presents the undamaged plate, and the red dash-dot line is for the hole-punctuated plate, and the magenta dashed line indicates the clay-attached plate for both in (a) and (b).46
- Figure 3-10: Histogram of each damage index. (a) Mean, (b) variance, (c) skewness, (d) kurtosis, (e) RMS of the undamaged plate (white histograms) and the hole punctuated plate (red histograms) for N=100.48
- Figure 3-11: Histogram of each damage index. (a) Mean, (b) variance, (c) skewness, (d) kurtosis, (e) RMS of the undamaged plate (white histograms) and the hole punctuated plate (red histograms) for N=50.49
- Figure 3-12: Histogram of each damage index. (a) Mean, (b) variance, (c) skewness, (d) kurtosis, (e) RMS of the undamaged plate (white histograms) and the clay attached plate (red histograms) for N=100.....50
- Figure 3-13: Histogram of each damage index. (a) Mean, (b) variance, (c) skewness, (d) kurtosis, (e) RMS of the undamaged plate (white histograms) and the clay attached plate (red histograms) for N=50.....51
- Figure 3-14: Data projected to first and second principal components in the undamaged and hole punctuated plate. The left plots show training data and the right plots represents test data in (a)-(c). The number of source N is 5, 50, and 100 for (a), (b), and (c), respectively. The circle and square markers show undamaged plates while the cross and star markers show damaged state (punctuated-hole).55
- Figure 3-15: Data projected to first and second principal components in the undamaged and clay attached plate. The left plots show training data and

the right plots represent test data in (a)-(c). The number of source N is 5, 50, and 100 for (a), (b) and (c), respectively. The circle and square markers show undamaged plates, while the cross and star markers show damaged state (clay-attached).....56

Figure 3-16: Result of SVM in projected data of $N=50$, (a) for the hole-punctuated case where the data are same with those of in Fig. 3-14(b), and (b) for the clay-attached case where the data are same with those of in Fig. 3-15 (b). The left plots show training data and the right plots represent test data in both (a) and (b). The circle and square markers express the undamaged plate, while the cross and star markers present the damaged state. The solid black line represents the linear hyperplane and the triangle markers with gray face color indicate the test errors.58

Figure 3-17: Averaged accuracy according to the number of sources. The blue dashed line presents the hole-punctuated plate, while the black solid line indicates the clay-attached plate.59

Figure 4-1: Process of severe slugging. (a) Slug formation, (b) slug movement into the separator, (c) blowout, (d) liquid fallback, and (e) pressure at the riser base during one cycle of severe slugging.73

Figure 4-2: Typical pressure signal near the riser base of DFSS. The water and gas superficial velocities are $u_{sw} = 0.15$ m/s and $u_{sg} = 0.99$ m/s, respectively. The period of the high-frequency element is approximately 20 s, and that of low-frequency part is roughly 100 s.75

Figure 4-3: Forces and moments on the small element of the pipe and of the corresponding fluid.....77

Figure 4-4: Experimental setup. (a) Location of accelerometer sensors, (b) photograph of the vertical riser, and (c) schematic diagram of the flow loop. The six sensor numbers are denoted as 1–6 in (a). The pipe is composed of PVC, and its inner diameter is 5.08 cm with a 5-mm thickness. The length of the inclined pipeline is 6.28 m at -15.9° to the horizontal and the height of the vertical riser is 5.6 m.80

Figure 4-5: . Measured pressure at the riser base for each flow regime: (a)–(c) SS1-1 at $u_{sw} = 0.09$ m/s with $u_{sg} = 0.59, 0.7,$ and 0.8 m/s; (d)–(f) SS1-2 at $u_{sw} = 0.19$ m/s with $u_{sg} = 0.59, 0.7,$ and 0.8 m/s; (g)–(i) irregular transition between SS3 and DFSS at $u_{sw} = 0.15$ m/s with $u_{sg} = 0.7, 0.8,$ and 0.99 m/s; (j)–(k) stable flow at $u_{sw} = 0.26$ m/s with $u_{sg} = 1.48$ and 1.97 m/s; and (l) controlled stable flow after SS1-1 generation at $u_{sw} =$

0.09 m/s with $u_{SG} = 0.7$ m/s.....	84
Figure 4-6: Comparison of the pressure at the riser base and the signals from accelerometer 1 for (a) SS1-1 at $u_{SW} = 0.09$ m/s with $u_{SG} = 0.59$ m/s and (b) SS1-2 at $u_{SW} = 0.19$ m/s with $u_{SG} = 0.59$ m/s. The black dotted line indicates the pressure and the blue solid line indicates the vibration.	85
Figure 4-7: Vibration signals from accelerometers 1–6 in (a)–(f), respectively. The flow is generated at $u_{SW} = 0.09$ m/s with $u_{SG} = 0.59$ m/s.....	87
Figure 4-8: Typical spectrum of FIV. The red dotted line presents the spectrum of FIV and the black solid line is the noise spectrum of the no-vibration part. Most energy of FIV is distributed below 10 kHz, especially near 1.5 kHz and 20 Hz.	88
Figure 4-9: Distribution of mean and variance features for stable flow ($u_{SW} = 0.26$ m/s, $u_{SG} = 1.48$ m/s) and SS1-1 ($u_{SW} = 0.09$ m/s, $u_{SG} = 0.59$ m/s). The red circle markers represent SS1-1 and the blue triangle markers represent stable flow.	92
Figure A-1: Averaged accuracy according to the number of sources without using PCA. The blue dashed line presents the hole-punctuated plate, while the black solid line indicates the clay-attached plate.....	112

List of Tables

Table 1-1: Comparison of SHM approaches.....	4
Table 1-2: Comparisons of sensing devices for unstable monitoring system. ...	7
Table 3-1: Summary of each damage index (DI). $f(t)$ is defined as $\frac{(\langle C_{12}(t) \rangle_N)^2}{\int_0^\infty (\langle C_{12}(t) \rangle_N)^2 dt}$	36
Table 3-2: Binary classification results of the SVM.	59
Table 4-1: Water and gas superficial velocities and the number of measured data according to the flow regime.	81
Table 4-2: Summary of feature parameters. $x(t)$ is defined as $x(t) = s(t) $ and $a_i(i-5)$ are the LPCs of Eq. (4.3).	90
Table 4-3: Binary classification results of the SVM.	96
Table 4-4: Binary classification results of the SVM for signals of length 7 s with six accelerometers.	97
Table 4-5: Binary classification results of the SVM including controlled stable regime.	98
Table 4-6: Multiclass classification results of the NN with six accelerometers.	100
Table A-1: Binary classification results of the SVM without using PCA.	112
Table A-2: The optimized parameters of binary classification results in Table 4-3.	113
Table A-3: The optimized parameters of binary classification results in Table 4-5.	114
Table A-4: The optimized parameters and probability of multiclass classification results for signals of 7 s in Table 4-6.	114
Table A-5: The optimized parameters and probability of multiclass classification results for signals of 5 s in Table 4-6.	115
Table A-6: The optimized parameters and probability of multiclass classification	

results for signals of 2.5 s in Table 4-6..... 115

Table A-7: Binary classification results with additional frequency domain features. 116

Chapter 1

Introduction

1.1. Structural health monitoring

Large structures such as ships, offshore structures, aircraft, bridges, buildings, and defense systems are essential structures in modern society. All these structures have a finite lifetime and degenerate after their initial operation. For safe operation and economic benefits, structural health monitoring (SHM) has been employed to detect damage at an early stage. SHM includes procedures of monitoring structures over time with proper measurements, extracting features sensitive to damage or unstable condition of structures, and determining the state of structures. In general, pattern recognition using machine learning algorithms is considered as the fundamental framework for SHM (Farrar and Worden, 2006; Farrar and Worden, 2012). The pattern recognition of SHM generates a connection between measured data and class labels by statistical modeling. It is mostly operated by four procedures (Farrar et al., 2001): (1) operational evaluation; (2) data acquisition; (3) feature selection; and (4) statistical modeling for feature discrimination.

Operational evaluation determines a monitoring target and techniques to be accomplished. In detail, it characterizes a type of damage to be investigated,

operational and environmental conditions, and limitations on data acquisition during operation. In the data acquisition stage, it decides a type, number, and location of sensors, the data acquisition system, and storage hardware. In this process, the characteristics of structures and economic issues should be considered. Based on the measured data, an important process of SHM is extracting features sensitive to the damage, which lead to discrimination between undamaged and damaged structures. The simple and low-dimensional features sensitive to the state of the structures are considered as ideal features. However, in many cases, more complicated signal processing would be necessary to extract effective features. For example, if the amplitude of time signals is too small to capture variations induced by the damage, using Fourier transform could be useful. And if the measured data are nonstationary, another transform processing such as wavelet transform can be advantageous. Among various feature extraction methods, it is important to select effective features considering the characteristics of structures. Lastly, statistical modeling for feature discrimination is performed using machine learning algorithms. This thesis explores vibration-based structural health monitoring using machine learning algorithms, damage detection in plate structure using the noise cross-correlation of diffuse fields (Chapter 3) and a new monitoring approach using accelerometers for severe slugging detection in the pipeline-riser system (Chapter 4).

1.2. Damage detection on the aluminum plate

Vibration-based damage detection approaches generally have been investigated using modal parameters, such as mode shape, mode frequency, and modal damping

(Farrar et al., 2001; Sabra et al., 2007). Since the damage can alter the physical properties of structures (e.g., mass, stiffness, and damping) which are related to modal parameters, the damage can be detected by analyzing the vibration response. The problem is that most damages are generated locally and could not significantly change the vibration response of structures, especially under ambient vibrations (Farrar et al., 2001; Farrar and Worden, 2012). Furthermore, passive monitoring using ambient vibrations could have difficulty in damage detection because of their random characteristics. For these reasons, many detection methods use acoustic, ultrasonic, magnetic, radiography, or eddy-current technique in practice (Doebeling et al., 1998; Shull, 2002). However, most of these techniques require active sensing systems, prior information about the probable location of damage, and direct access for inspection (Farrar and Worden, 2012; Sabra et al., 2007).

In recent years, a series of studies on ambient noise interferometry have been developed, which demonstrate that the time-domain Green's function (TDGF) can be extracted from the cross-correlation of ambient diffuse fields (Lobkis and weaver, 2001; Roux and Kuperman, 2004; Sabra et al., 2005; Snieder, 2002; Weaver and Lobkis, 2004). These studies have two advantages in SHM application: (1) active sources are not required, while only passive sensors are sufficient for damage detection; and (2) the random characteristics generated by multiple reflections of complex structures are no longer a drawback, because the method uses randomness of the wave field (Jung et al., 2018; Sabra et al., 2007; Sabra et al., 2008). The detailed description of advantages and limitations are presented in Table 1-1 with comparisons of conventional active and passive approaches. Experimental studies of the ambient noise interferometry have been explored in various structures: a stainless steel flat plate and a hydrofoil installed in a cavitation tunnel under turbulent flow

induced vibration (Sabra et al., 2007); aluminum plate using random excitations of a Garnet pulsed laser (Sabra et al., 2008); aluminum plate with two actuators and a scanning laser Doppler vibrometer (Duroux et al., 2010); and aluminum plate with random excitation generated by the shaker (Tippmann et al., 2014; Tippmann and Lanza di Scalea, 2015). Its application to SHM was investigated by Tippmann and Lanza di Scalea (2014), which adopted the K-nearest neighbor (KNN) algorithm to detect nonlinear material attachment on the plate.

Table 1-1: Comparison of SHM approaches.

SHM	Advantage	Limitations
Active	<ul style="list-style-type: none"> • Possible in local damage detection • Stable control of source operation 	<ul style="list-style-type: none"> • Required deployment of an active source (power consumption) • Prior information about probable locations • Requirement for direct access for inspection • Offline monitoring (inspection)
Passive	<ul style="list-style-type: none"> • Possible in real-time monitoring • Possible in tracking global response of structures 	<ul style="list-style-type: none"> • Difficult for detecting damage of local phenomenon • Can be contaminated by random noise
NCF using diffuse fields	<ul style="list-style-type: none"> • Means to perform SHM without local (active sources) • Possible in real-time monitoring • Possible in local damage detection 	<ul style="list-style-type: none"> • Diffuse field is preferable

This dissertation explores a developed experiment applying the noise cross-correlation function of diffuse fields. We extend these methods to detect two types of damages on an aluminum plate. To generate more suitable environmental conditions for marine and offshore structures exposed to wave impacts (e.g., slamming), a hand-held impact hammer is used as the source. Furthermore, various

environmental conditions are considered by changing the number and location of sources. To extract damage sensitive features, several statistics are obtained from the noise cross-correlation function. And a linear support vector machine (SVM) is adopted to classify an undamaged plate and damaged plate. The method is validated even in a less diffuse field produced by a small number of sources. The outline of the process is presented in Fig. 1-1.

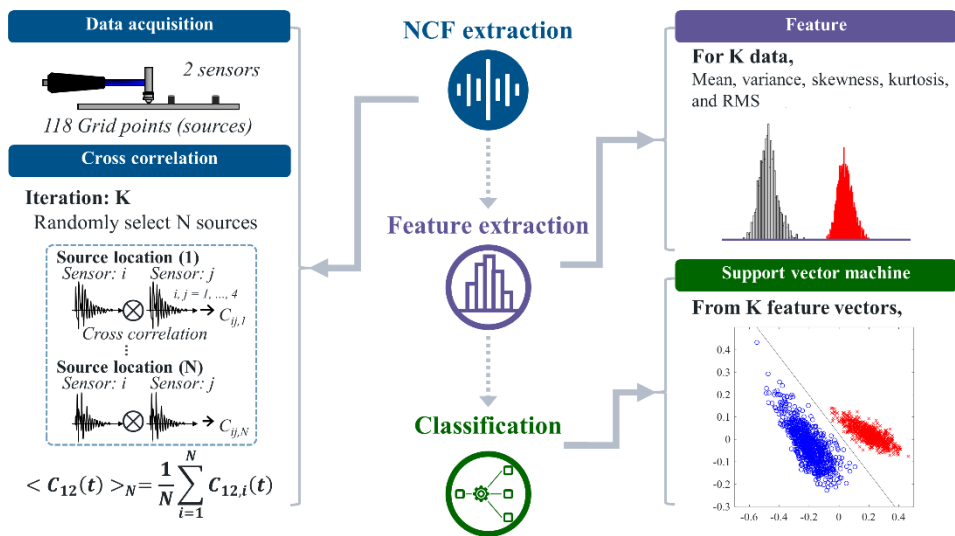


Figure 1-1: Outline of damage detection in the plate structure.

1.3. Severe slugging detection in the pipeline-riser system

In unstable flow monitoring of the pipeline-riser system, many researchers have been interested in early recognition of unstable flow, severe slugging. It can be produced in an undesired cycle with unstable blowout, which results in negative effects to structures such as fatigue, increased corrosion, liquid overflow, and low production (Hill et al., 1994; Pedersen et al., 2017; Sun and Jepson, 1992). Goudinakis (2004) investigated multiphase flow identification in the pipeline-riser system using normalized differential pressures. A neural network (NN) was applied to classify four classes of bubble, oscillation, slug, and severe slugging. Ye and Guo (2013) acquired differential pressure signals in the S-shaped riser and trained the least-squares SVM (LS-SVM) to identify severe slugging 1, severe slugging 2, severe slugging transition, oscillation, and stable flow. Zou (2017) measured the differential pressure in the pipeline-riser system and adopted the LS-SVM with simple features for fast recognition.

The pressure gauge used in the aforementioned studies is low-cost and usable at wide ranges of pressures and temperatures. However, it has some drawbacks: (1) a pressure tap can be blocked; (2) a pressure signal can be affected not only by the flow regime but also by the phases' velocity (Rosa et al., 2010); and (3) it is difficult to move into another location after its installation. In addition to the pressure gauge, the use of impedance sensors has an advantage in computational cost because its output is proportional to the void fraction which is closely related to the flow pattern (Rosa et al., 2010). However, it has limitations for several reasons: it is only applicable to two-phase flow, where the conductivities and dielectric coefficients of the gas and liquid are significantly different from each other (Wu et al., 2001); it is

sensitive to temperature; and it is only available for pipe composed of non-conducting material. For these reasons, its application in the industrial field can be difficult.

This dissertation proposes a new monitoring approach for the pipeline-riser structure based on vibration signals using accelerometers. We focused on the advantages of the accelerometer: it can be operated in nonintrusive fashion; it can be transferred to other locations after its installation according to the user’s desire or operational purpose; and the vibration characteristics are significantly different between stable flow and unstable flow. These motivate our research to use accelerometers for severe slugging detection and to consider applications in real-time monitoring. The characteristics of sensing devices are summarized in Table 1-2.

Table 1-2: Comparisons of sensing devices for unstable monitoring system.

Sensor	Advantage	Limitations
Pressure gauge	<ul style="list-style-type: none"> • Low-cost • Usable at wide ranges of pressures and temperatures 	<ul style="list-style-type: none"> • Pressure tap can be blocked • Can be affected by either the water’s or gas’s velocity as well as by the flow regime (Rosa et al., 2010) • Difficult to move into another location after the installation
Impedance sensor	<ul style="list-style-type: none"> • Relatively low computational cost because of the signal’s output proportional to the void fraction (Rosa et al., 2010) 	<ul style="list-style-type: none"> • Only applicable to two-phase flow • Sensitive to temperature (Wu et al., 2010) • Requires that the pipe should be composed of non-conducting material
Accelerometer	<ul style="list-style-type: none"> • Usable in nonintrusive way • Can be transferred after the initial installation • Usable at wide ranges of temperatures 	<ul style="list-style-type: none"> • Can be contaminated by vortex induced vibration or wave motion • Need for low noise cable (for charge type accelerometer)

In this dissertation, severe slugging detection is performed using vibration signals from six accelerometers installed at the vertical riser. Simple statistics and linear prediction coefficients (LPC) are extracted from the vibration signals. The SVM is employed for binary classification and the NN is applied for multiclass classification. Severe slugging is recognized according to the signal length and location of sensors. The outline of the process is demonstrated in Fig. 1-2.

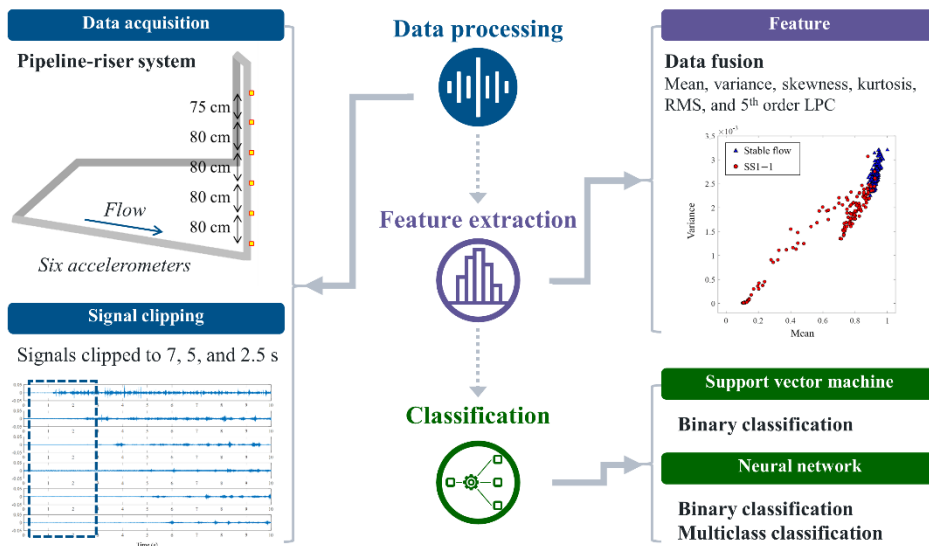


Figure 1-2: Outline of unstable flow monitoring in the pipeline-riser system.

1.4. Organization of the Dissertation

The remainder of this dissertation is organized as follows. In chapter 2, machine learning algorithms used in this dissertation, principal component analysis (PCA), SVM, and NN are presented. In chapter 3, the experimental study of damage

detection on the plate structure using the cross-correlation of diffuse fields is demonstrated. In chapter 4, the experimental research on early recognition of severe slugging in the pipeline-riser system with accelerometers is investigated. Chapter 5 concludes this dissertation with contributions of the research.

Bibliography

Doebbling, S. W., Farrar, C. R., Prime, M. B., 1998. A summary review of vibration-based damage identification methods. *Shock. Vib. Dig.* 30 (2), 91–105.

Farrar, C. R., Doebbling, S. W., and Nix, D. A., 2001. Vibration-based structural damage identification. *Philos. Trans. R. Soc. A Math. Phys. Eng. Sci.* 359 (1778), 131–149.

Farrar, C. R., and Worden, K., 2006. An introduction to structural health monitoring. *Philosophical Transactions of the Royal Society A: Mathematical, Physical and Engineering Sciences*, 365 (1851), 303-315.

Farrar, C. R., Worden, K., 2012. *Structural health monitoring: a machine learning perspective*. John Wiley & Sons.

Goudinakis, G., 2004. Investigation on the use of raw time series and artificial neural networks for flow pattern identification in pipelines. Cranfield University, Ph.D. thesis.

Hill, T.J., Wood, D.G., 1994. Slug flow: occurrence, consequences, and prediction. In: *University of Tulsa Centennial Petroleum Engineering Symposium*.

Jung, S., Seong, W., and Lee, K., 2018. Damage detection on an aluminum plate from the cross-correlation of diffuse field using the support vector machine.

Ocean Engineering, 161, 88-97.

Lobkis, O.I., Weaver, R.L., 2001. On the emergence of the Green's function in the correlations of a diffuse field. *J. Acoust. Soc. Am.* 110 (6), 3011–3017.

Murphy, K. P., 2012. *Machine learning: a probabilistic perspective*. MIT press.

Pedersen, S., Durdevic, P., Yang, Z., 2017. Challenges in slug modeling and control for offshore oil and gas productions: a review study. *Int. J. Multiph. Flow* 88, 270–284.

Rosa, E.S., Salgado, R.M., Ohishi, T., Mastelari, N., 2010. Performance comparison of artificial neural networks and expert systems applied to flow pattern identification in vertical ascendant gas-liquid flows. *Int. J. Multiph. Flow* 36, 738–754.

Roux, P., Kuperman, W.A., 2004. Extracting coherent wave fronts from acoustic ambient noise in the ocean. *J. Acoust. Soc. Am.* 116 (4), 1995–2003.

Sabra, K.G., Roux, P., Kuperman, W.A., 2005. Arrival-time structure of the time-averaged ambient noise cross-correlation function in an oceanic waveguide. *J. Acoust. Soc. Am.* 117 (1), 164–174.

Sabra, K.G., Winkel, E.S., Bourgoyne, D. a, Elbing, B.R., Ceccio, S.L., Perlin, M., Dowling, D.R., 2007. Using cross correlations of turbulent flow-induced

ambient vibrations to estimate the structural impulse response. Application to structural health monitoring. *J. Acoust. Soc. Am.* 121 (4), 1987–1995.

Sabra, K.G., Srivastava, A., Lanza di Scalea, F., Bartoli, I., Rizzo, P., Conti, S., 2008. Structural health monitoring by extraction of coherent guided waves from diffuse fields. *J. Acoust. Soc. Am.* 123 (1), EL8–EL13.

Shull, P. J. 2002. *Nondestructive evaluation: theory, techniques, and applications.* CRC press.

Snieder, R., 2002. Coda wave interferometry for estimating nonlinear behavior in seismic velocity. *Science* 295, 2253–2255.

Sun, J.Y., Jepson, W.P., 1992. Slug flow characteristics and their effect on corrosion rates in horizontal oil and gas pipelines. In: *Annual Technical Conference and 11 Exhibition of the Society of Petroleum Engineers.*

Tippmann, J., Zhu, X., Scalea, F., 2014. Probabilistic structural health monitoring using passive-only damage detection by reciprocity of Green's function reconstructed from diffuse acoustic fields. In: *EWSHM-7th European Workshop on Structural Health Monitoring.*

Tippmann, J.D., Lanza di Scalea, F., 2015. Passive-only damage detection by reciprocity of Green's functions reconstructed from diffuse acoustic fields with application to wind turbine blades. *J. Intell. Mat. Syst. Struct.* 26 (10), 1251–1258.

- Wapenaar, K., 2004. Retrieving the elastodynamic Green's function of an arbitrary inhomogeneous medium by cross correlation. *Phys. Rev. Lett.* 93, 254301.
- Wu, H., Zhou, F., Wu, Y., 2001. Intelligent identification system of flow regime of oil gas-water multiphase flow. *Int. J. Multiph. Flow* 27, 459–475.
- Ye, J., Guo, L., 2013. Multiphase flow pattern recognition in pipeline-riser system by statistical feature clustering of pressure fluctuations. *Chem. Eng. Sci.* 102, 486–501.
- Zou, S., Guo, L., Xie, C., 2017. Fast recognition of global flow regime in pipeline-riser system by spatial correlation of differential pressures. *Int. J. Multiph. Flow* 88, 222–237.

Chapter 2

Machine learning algorithms for structural health monitoring

For monitoring intact and stable condition of the structure, classification analysis is performed using machine learning algorithms. Machine learning analyzes patterns of data and makes the decision about unknown data of the structure. In this thesis, SVM and NN are used for classification analysis. An important factor in machine learning is extracting damage-sensitive features. Many types of features can be generated according to characteristics of data, such as comparing data waveforms, power spectral density functions, or cross-spectral density functions (Farrar et al., 2012). Commonly used and simple damage-sensitive features of statistic parameters and linear prediction coefficients are applied in this study. Specific descriptions of features used for the plate and pipeline-riser system are provided in Chapters 3 and 4, respectively. In this chapter, machine learning algorithms for classification analyses are described. The PCA of dimensionality reduction algorithm is explained in Section 2.1. Learning algorithms, SVM and NN are presented in Sections 2.2 and 2.3, respectively.

2.1. Principal component analysis (PCA)

Dealing with high dimensional data, it is important to extract the important structure of data distribution. The objective of PCA is to analyze the main characteristics of data by reducing the dimension of data composed of interrelated variables. It makes the set of correlated variables into the data with a smaller number of representative variables (Bishop, 2006; James et al., 2013). In this study, the PCA is adopted for data visualization and classification in Chapter 3. PCA uses an orthogonal transformation to make a lower uncorrelated dimension, which are called the principal components (PCs). PCs are generated by maximizing the variance of the projected data which is equivalent to minimizing projection residuals. When the data \mathbf{x}_n , ($n = 1, \dots, N$) with dimension D are projected to direction of \mathbf{u}_1 corresponding to one-dimensional space, the objective of PCA is to find \mathbf{u}_1 maximizing the variance as indicated by the red long arrow in Fig. 2-1.

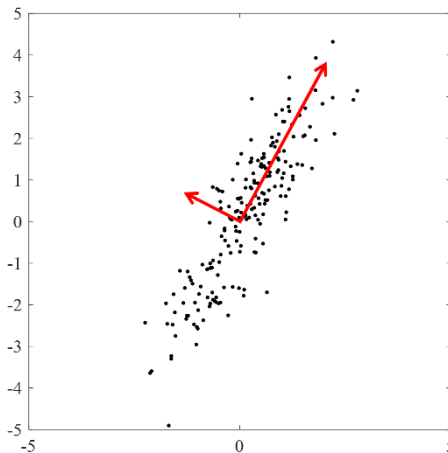


Figure 2-1: Samples of multivariate Gaussian distribution centered at (0, 0) with a

covariance matrix $\begin{bmatrix} 1 & 1.5 \\ 1.5 & 3 \end{bmatrix}$.

The projected data onto \mathbf{u}_1 is $\mathbf{u}_1^T \mathbf{x}_n$. If the mean of projected data is $\bar{\mathbf{x}}$, the variance of the projected data can be expressed as

$$\frac{1}{N} \sum_{n=1}^N \{ \mathbf{u}_1^T \mathbf{x}_n - \mathbf{u}_1^T \bar{\mathbf{x}} \}^2 = \frac{1}{N} \sum_{n=1}^N \mathbf{u}_1^T (\mathbf{x}_n - \bar{\mathbf{x}}) (\mathbf{x}_n - \bar{\mathbf{x}})^T \mathbf{u}_1 = \mathbf{u}_1^T \mathbf{S} \mathbf{u}_1, \quad (2.1)$$

where $\mathbf{S} = \frac{1}{N} \sum_{n=1}^N (\mathbf{x}_n - \bar{\mathbf{x}}) (\mathbf{x}_n - \bar{\mathbf{x}})^T$ is a covariance matrix. The objective function of maximizing the variance $\mathbf{u}_1^T \mathbf{S} \mathbf{u}_1$ with the constraint $\mathbf{u}_1^T \mathbf{u}_1 = 1$ can be presented using Lagrange multiplier λ_1 as

$$L = \mathbf{u}_1^T \mathbf{S} \mathbf{u}_1 + \lambda_1 (1 - \mathbf{u}_1^T \mathbf{u}_1). \quad (2.2)$$

Calculating the derivative with respect to \mathbf{u}_1 equals to zero results in

$$\mathbf{S} \mathbf{u}_1 = \lambda_1 \mathbf{u}_1. \quad (2.3)$$

Therefore, \mathbf{u}_1 is an eigenvector of \mathbf{S} . And the variance becomes maximum when \mathbf{u}_1 is an eigenvector with the largest eigenvalue λ_1 , which is the first PC. Next, the PCA finds the second PC orthogonal to the first PC. The second PC has second

largest variance, and the subsequent PCs are calculated in the same way (Morrison et al., 1998). From Eq. (2.3), all PCs (eigenvectors) are produced by using singular value decomposition (SVD). The subsequent PCs have succeeding largest eigenvalues.

Reducing the dimension of data, it is important to represent the original data with lower dimension without critical information loss. To select m PCs from the original data, the cumulative percentage of total variation t_m is applied as (Jolliffe, 2002)

$$t_m = 100 \times \frac{\sum_{i=1}^m \lambda_i}{\sum_{i=1}^p \lambda_i}, \quad (2.4)$$

where λ_i is the i^{th} largest eigenvalue, and p and m are the number of variables in original data and the number of selected eigenvalues, respectively. The t_m is an index of the number of m largest eigenvalues explaining the total variation of the original data. It can be defined by user's desire such as 80% or 90%. The number of PCs is the smallest value m , which exceeds the determined percentage. In this dissertation, the t_m is chosen as 90%.

2.2. Support vector machine (SVM)

In this study, the machine learning algorithm SVM is adopted for binary classification. The SVM is a supervised learning algorithm which maximizes a margin, the smallest distance between the hyperplane and any of the data (Bishop,

2006). The hyperplane is dependent on sparse solutions, a subset of training data called support vectors. An advantage of SVM is that the objective function is convex where every local minimum is a global minimum.

Linear SVM

The linear SVM uses models of

$$y(\mathbf{x}) = \mathbf{w}^T \mathbf{x} + b, \quad (2.5)$$

where \mathbf{x}_n are input vectors with class targets t_n labeled as 1 or -1 . For convenience, assume that data of $t_n = +1$ have $y(\mathbf{x}_n) > 0$ and those of $t_n = -1$ have $y(\mathbf{x}_n) < 0$ as shown in Fig. 2-2. All dataset satisfy $t_n y(\mathbf{x}_n) > 0$. Among many solutions for separating classes, the hyperplane called as decision boundary is determined as maximizing the margin. The margin is the perpendicular distance between the data point \mathbf{x} and the hyperplane $y(\mathbf{x}) = 0$ calculated as $|y(\mathbf{x})| / \|\mathbf{w}\|$. Therefore, the distance of correctly classified data \mathbf{x}_n with target t_n from the hyperplane can be expressed as

$$\frac{t_n y(\mathbf{x}_n)}{\|\mathbf{w}\|} = \frac{t_n (\mathbf{w}^T \mathbf{x}_n + b)}{\|\mathbf{w}\|}. \quad (2.6)$$

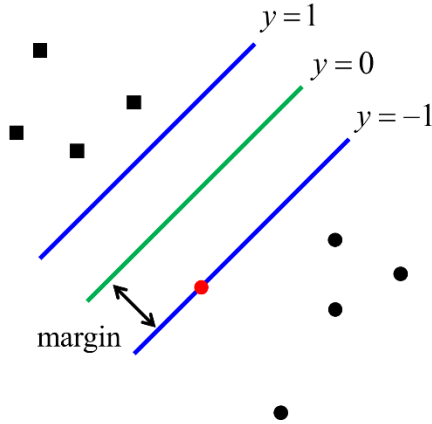


Figure 2-2: Example of data distribution composed of two-classes. Data of $t_n = +1$ are presented as square markers and have $y(\mathbf{x}_n) > 0$. And data of $t_n = -1$ are described as circle markers and have $y(\mathbf{x}_n) < 0$. The margin is the distance between the hyperplane of green solid line and a red circle marker of $t_n = -1$.

By adopting proper rescaling constant, the data closest to the hyperplane can be expressed as $t_n(\mathbf{w}^T \mathbf{x}_n + b) = 1$, where the data satisfying the equality are defined as support vectors producing the hyperplane. Accordingly, all data satisfy the constraints

$$t_n(\mathbf{w}^T \mathbf{x}_n + b) \geq 1. \tag{2.7}$$

Maximizing the margin $1/\|\mathbf{w}\|$ is equivalent to minimizing $\|\mathbf{w}\|^2$. Therefore, the optimization problem becomes

$$\underset{\mathbf{w}, b}{\operatorname{argmin}} \frac{1}{2} \|\mathbf{w}\|^2 \quad \text{subject to } t_n (\mathbf{w}^\top \mathbf{x}_n + b) \geq 1. \quad (2.8)$$

Lagrange multipliers α_n are applied to solve the constrained optimization problem of Eq. (2.8). Then the Lagrangian function is

$$L(\mathbf{w}, b, \boldsymbol{\alpha}) = \frac{1}{2} \|\mathbf{w}\|^2 - \sum_{n=1}^N \alpha_n \{t_n (\mathbf{w}^\top \mathbf{x}_n + b) - 1\}. \quad (2.9)$$

where $\boldsymbol{\alpha} = (\alpha_1, \dots, \alpha_N)^\top$. Calculating the derivatives of $L(\mathbf{w}, b, \boldsymbol{\alpha})$ with respect to \mathbf{w} and b equal to zero, two equations are obtained as

$$\frac{\partial L(\mathbf{w}, b, \boldsymbol{\alpha})}{\partial \mathbf{w}} = 0 \rightarrow \mathbf{w} = \sum_{n=1}^N \alpha_n t_n \mathbf{x}_n \quad (2.10)$$

$$\frac{\partial L(\mathbf{w}, b, \boldsymbol{\alpha})}{\partial b} = 0 \rightarrow \sum_{n=1}^N \alpha_n t_n = 0. \quad (2.11)$$

From Eqs. (2.10) and (2.11), Eq. (2.9) can be re-expressed by dual representation as

$$\tilde{L}(\boldsymbol{\alpha}) = \sum_{n=1}^N \alpha_n - \frac{1}{2} \sum_{n=1}^N \sum_{m=1}^N \alpha_n \alpha_m t_n t_m \mathbf{x}_n^\top \mathbf{x}_m, \quad (2.12)$$

with constraints $\alpha_n \geq 0$, $n = 1, \dots, N$ and $\sum_{n=1}^N \alpha_n t_n = 0$.

Meanwhile, if the data distribution is not separable, some misclassified training

data need to be allowed to achieve generalization. As shown in Fig. 2-3, data of circle markers with external line are on the opposite side of the margin boundary $y = -1$. To make appropriate penalty according to the distance from the margin boundary, slack variables $\xi_n \geq 0$, $n = 1, \dots, N$ are introduced. The slack variables ξ_n are 0 for data on the correct side of the margin boundary. ξ_n are between 0 and 1 for data between the hyperplane and the margin boundary, as shown as circle marker with external yellow solid line in Fig. 2-3. And the misclassified samples have $\xi_n > 1$, presented as a circle marker with external red dashed line in Fig. 2-3. If the data are on the hyperplane, they have $\xi_n = 1$.

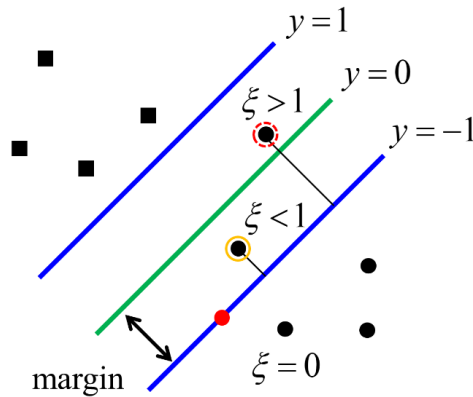


Figure 2-3: Example of data distribution composed of two-classes with misclassified samples. Data of $t_n = +1$ are presented as square markers, and data of $t_n = -1$ are described as circle markers. Misclassified sample of circle marker with red dashed line has $\xi_n > 1$.

Accordingly, the constraint is changed to $t_n (\mathbf{w}^T \mathbf{x}_n + b) \geq 1 - \xi_n$, and the objective

function is to minimize

$$C \sum_{n=1}^N \xi_n + \frac{1}{2} \|\mathbf{w}\|^2, \quad (2.13)$$

where the parameter C indicates the trade-off between the margin maximization and the penalty of misclassification. For example, larger C increases the weight on misclassified samples and results in stricter separation with fewer support vectors.

The Lagrangian function with slack variables becomes

$$L(\mathbf{w}, b, \boldsymbol{\alpha}) = \frac{1}{2} \|\mathbf{w}\|^2 + C \sum_{n=1}^N \xi_n - \sum_{n=1}^N \alpha_n \left\{ t_n (\mathbf{w}^T \mathbf{x}_n + b) - 1 + \xi_n \right\} - \sum_{n=1}^N \mu_n \xi_n, \quad (2.14)$$

where α_n and μ_n are Lagrange multipliers. According to dual representations, the problem is to minimize

$$\tilde{L}(\boldsymbol{\alpha}) = \sum_{n=1}^N \alpha_n - \frac{1}{2} \sum_{n=1}^N \sum_{m=1}^N \alpha_n \alpha_m t_n t_m \mathbf{x}_n^T \mathbf{x}_m, \quad (2.15)$$

subject to

$$0 \leq \alpha_n \leq C, \quad n = 1, \dots, N \quad (2.16)$$

$$\sum_{n=1}^N \alpha_n t_n = 0. \quad (2.17)$$

Eq. (2.15) is same as Eq. (2.12) of separable data distribution except for the constraints.

Nonlinear SVM

The nonlinear SVM uses model of $y(\mathbf{x}) = \mathbf{w}^T \phi(\mathbf{x}) + b$. It is based on linear combinations of a kernel function with nonlinear feature space mapping function $\phi(\mathbf{x})$. The kernel function is expressed as

$$k(\mathbf{x}, \mathbf{x}') = \phi(\mathbf{x})^T \phi(\mathbf{x}'). \quad (2.18)$$

For example, the linear kernel is $k(\mathbf{x}, \mathbf{x}') = \mathbf{x}^T \mathbf{x}'$, where $\phi(\mathbf{x}) = \mathbf{x}$. The kernel function formulated by inner product allows to replace the inner product of input vectors \mathbf{x} with the kernel function composed of other mapping functions. The terms of inner product in Eqs. (2.12) and (2.15), $\mathbf{x}_n^T \mathbf{x}_m$ can be changed to other kernel function by the kernel trick. Therefore, the kernel-based SVM also can have sparse solutions of kernel function, calculated from the subset of training data. Eqs. (2.12) and (2.15) can be expressed as

$$\tilde{L}(\boldsymbol{\alpha}) = \sum_{n=1}^N \alpha_n - \frac{1}{2} \sum_{n=1}^N \sum_{m=1}^N \alpha_n \alpha_m t_n t_m k(\mathbf{x}_n, \mathbf{x}_m). \quad (2.19)$$

In general, a polynomial kernel of degree p $k(\mathbf{x}, \mathbf{y}) = (\mathbf{x} \cdot \mathbf{y} + 1)^p$ or a radial basis

function (RBF) $k(\mathbf{x}, \mathbf{y}) = \exp\left(-\|\mathbf{x} - \mathbf{y}\|^2 / 2\sigma^2\right)$ is used.

The SVM is basically a binary classifier algorithm. However, it can be applied for multiclass classification by using the one-versus-rest method or one-versus-one approach. Instead of applying these approaches, the NN is adopted for multiclass classification in this study.

2.3. Neural network (NN)

In this dissertation, NN is applied for multiclass classification. It is based on function

$$y(\mathbf{x}, \mathbf{w}) = f\left(\sum_{j=1}^M w_j \phi_j(\mathbf{x})\right), \quad (2.20)$$

where $f(\cdot)$ is a nonlinear activation function and $\phi_j(\mathbf{x})$ are nonlinear basis functions. The output is linear combinations of $\phi_j(\mathbf{x})$, which are composed of the inputs.

The structure of basic NN is illustrated in Fig. 2-4. The unit of hidden layer is composed of M linear combinations of the inputs x_1, x_2, \dots, x_D , expressed as

$$a_j = \sum_{i=1}^D w_{ji}^{(1)} x_i + w_{j0}^{(1)}, \quad (2.21)$$

where $j = 1, \dots, M$, M is the number of units of the hidden layer, $w_{ji}^{(1)}$ present weights, $w_{j0}^{(1)}$ indicate biases, and the superscript (1) presents the first layer of the structure. The activations a_j are transformed by a differentiable and nonlinear activation function $h(\cdot)$ as $z_i = h(a_j)$, which are called as hidden units. Various functions such as logistic sigmoid function or tangent hyperbolic function can be used as nonlinear activation functions. Lastly, the output unit activations are calculated from values of hidden units

$$a_k = \sum_{j=1}^M w_{kj}^{(2)} z_j + w_{k0}^{(2)}, \quad (2.22)$$

where $k = 1, \dots, K$, K is the number of outputs, and $w_{k0}^{(2)}$ present biases.

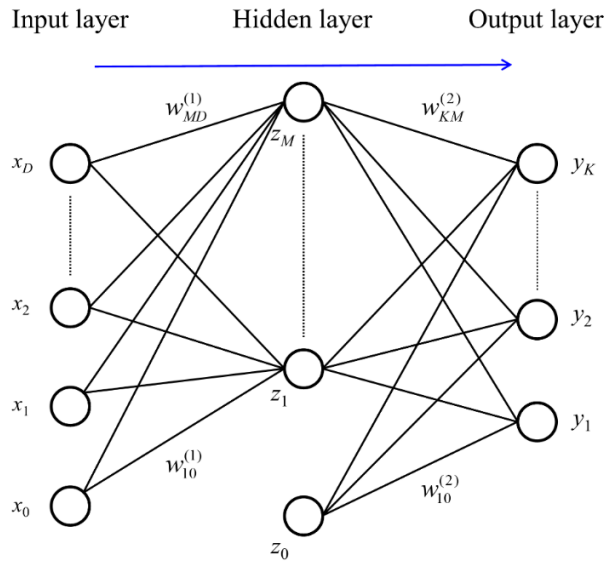


Figure 2-4: Structure of basic feedforward NN. It has D inputs, M units of hidden

layer, and K outputs.

The outputs y_k are generated using an appropriate activation function operated on the output unit activations. Integrating the aforementioned process, the final outputs are presented as

$$y_k(\mathbf{x}, \mathbf{w}) = h \left(\sum_{j=1}^M w_{kj}^{(2)} h \left(\sum_{i=1}^D w_{ji}^{(1)} + w_{j0}^{(1)} \right) + w_{k0}^{(2)} \right). \quad (2.23)$$

By absorbing bias parameters by introducing the input variable $x_0 = 1$, the NN function can be expressed as

$$y_k(\mathbf{x}, \mathbf{w}) = h \left(\sum_{j=0}^M w_{kj}^{(2)} h \left(\sum_{i=0}^D w_{ji}^{(1)} \right) \right). \quad (2.24)$$

The NN model of Eq. (2.24) is composed of two process, two-layer network as shown in Fig. 2-4. The more general structure of NN can be generated by additional layers. In this dissertation, only a feed-forward architecture without closed directed cycles is used.

Bibliography

Bishop, C., 2006. Pattern recognition and machine learning. Springer-Verlag, New York.

Farrar, C. R., Worden, K., 2012. Structural health monitoring: a machine learning perspective. John Wiley & Sons.

James, G., Witten, D., Hastie, T., and Tibshirani, R., 2013. An introduction to statistical learning. New York: springer.

Jolliffe, I.T., 2002. Principal Component Analysis. John Wiley & Sons, Ltd.

Morrison, D.F., 1998. Multivariate Analysis, Overview. John Wiley & Sons, Ltd.

Chapter 3

Damage detection on the aluminum plate

Abstract

In order to assess the damage detectability of the structural health monitoring method using diffuse fields, a laboratory experiment is conducted on an aluminum plate where two accelerometers are mounted as receivers. Two types of damages, a nonlinear material attachment and a punctuated hole, are considered. A hand-held impact hammer is used for the excitation, whereby the hammer is moved over grid points drawn on the aluminum plate, and thus the diffuse fields are generated by superposing the wave fields by many excitations randomly sampled. From the cross-correlation of diffuse fields between two receivers, we extract the coherent wave field in cases with and without damages. To detect the damage, a novel damage detection algorithm using a support vector machine is suggested based on the reduced features, transformed from several statistical parameters of damaged and undamaged noise cross-correlation functions, aided by the principal component analysis. The performance of the proposed algorithm is analyzed for the number of sources and damage types.

3.1. Introduction

Structural health monitoring (SHM) is imperative for safe operation of large structures such as ships, offshore structures, and bridges. Traditionally, the SHM is classified into two groups: active and passive method. The active SHM method detects damages using signals generated by active sources and the passive method only uses ambient signals received by passive sensors to find damages (Davis and Bockhurst, 2015; Farrar and Worden, 2007; Jamalikia et al., 2016; Liu et al., 2017; Yi, 2016).

Recently, a series of studies on ambient noise interferometry have demonstrated that the time-domain Green's function (TDGF) between two receiving points can be reconstructed from the ensemble average of the cross-correlation of ambient diffuse fields (Lobkis and Weaver, 2001; Roux and Kuperman, 2004; Sabra et al., 2005; Snieder, 2002; Wapenaar, 2004; Weaver and Lobkis, 2004). These interesting studies have two implications for the application to the SHM in the plate structure. First, active sensors are not needed for SHM and a pair of passive sensors is sufficient for the recovery of TDGF if the inspected plate creates sufficient diffuse field. Second, in the ambient noise interferometry, the plate structure causing multiple reflections is no longer a hindrance to the SHM since the complexity of the structure rather promotes the diffuseness and randomness of the wave field.

Applications of the ambient noise interferometry to the SHM of the plate structure were first investigated by Sabra et al. (2007). They performed an experiment for a flat plate and a hydrofoil in a cavitation tunnel and reconstructed the TDGF from ambient vibrations induced by turbulent flows. Successively, Sabra et al. (2008) extracted the TDGF in an aluminum plate from the diffuse field

generated by random excitations of a Garnet pulsed laser and observed the change of TDGF with and without a hole damage. Duroux et al. (2010) performed similar experimental work on an aluminum plate with two piezoelectric actuators and a scanning laser Doppler vibrometer. They synthesized the diffuse field with multiple measurements based on the source-receiver reciprocity and conducted several theoretical and experimental analyses. Recently, experimental studies were investigated to detect a nonlinear material attachment on the plate (Tippmann et al., 2014; Tippmann and Lanza di Scalea, 2015). The diffuse field needed to obtain the TDGF is artificially made from multiple excitations by the shaker over 576 grid points on the plate. They defined several damage indices (DIs), describing the similarity of forward and backward TDGF, that are expected to be sensitive to the damage with nonlinear behavior (Sohn et al., 2004; Tippmann and Lanza di Scalea, 2015). These DIs were used for the K nearest neighbor (KNN) algorithm with the principal component analysis (PCA) to detect the damage, and showed good damage detectability.

In this chapter, we perform an experimental study on the passive SHM from a diffuse field on an aluminum plate and propose a novel damage detection algorithm using statistical parameters of damaged and undamaged noise cross-correlation functions (NCFs). The experimental procedure of Tippmann and Lanza di Scalea (2015) is adopted in this dissertation. However, the approach in this study differs from that by Tippmann and Lanza di Scalea (2015) in a number of ways as follows. (1) Instead of the random noise shaker, a hand-held impact hammer is used as the source. In practice, while the use of natural random noise may be more cost-effective, it renders the stable control of the SHM difficult. It can be suitable for marine system or offshore system, which is usually exposed to wave impact loading (e.g.,

slamming). In this dissertation, the effects of number of the sources on the damage detection are studied. (2) In addition to nonlinear material attachment considered in Tippmann and Lanza di Scalea (2015), a punctuated hole damage is used. (3) New feature vectors characterizing the elastic behavior of the plate are presented based on the statistics of the damaged and undamaged data of the NCF. These feature vectors differ from current feature vectors using the reciprocity of TDGF, and are applicable to all types of damages. The PCA is used to reduce the dimension of the feature vectors and the support vector machine (SVM) is then applied for damage detection.

This chapter is organized as follows: Section 3.2 summarizes the theoretical background of the extraction of the coherent fields from the cross-correlation of the diffuse field. In addition, a few statistical parameters using the NCF are given for damage detection. Section 3.3 describes the laboratory experiment for two cases of nonlinear attachment and hole damage and measurement data. The damage detection using the SVM with the PCA is given in Section 3.4. Section 3.5 is a summary and conclusions of this chapter.

3.2. Theoretical background

Extraction of coherent fields from the diffuse field generated by a number of sources

As shown in Fig. 3-1, consider the elastic field generated by a source arbitrarily located over the structure at N points. The cross-correlation of the signals received at two receivers is defined as (Duroux et al., 2010)

$$C_{12,i}(t) = \int_0^T s_{1,i}(\tau) s_{2,i}(t + \tau) d\tau, \quad (3.1)$$

where $s_{m,i}(t)$ is the signal acquired at sensor m ($m=1, 2$) from a source located on the i^{th} position of the structure in time $[0, T]$ (Bendat and Piersol, 2011). The averaged NCF for the N excitations is expressed as (Duroux et al., 2010)

$$\langle C_{12}(t) \rangle_N = \frac{1}{N} \sum_{i=1}^N C_{12,i}(t), \quad (3.2)$$

where the operator $\langle \dots \rangle_N$ refers to the ensemble averaging of N cross-correlation functions. It has been demonstrated that, when the N sources are uniformly distributed in space and time and the resultant field is fully diffused, the TDGF is reconstructed from the time derivative of Eq. (3.2). However, the real environment is not ideal, since many of the noise sources have a band-limited spectrum and their distribution is not always uniform in space and time. The loss is always present in the structure and the receivers have their own transducer response characteristics. Considering such factors, the averaged NCF can be theoretically stated as (Roux et al., 2005)

$$\langle C_{12}(t) \rangle_N \approx Q(t) * [G_{12}(t) - G_{21}(-t)], \quad (3.3)$$

where $G_{12}(t)$ is the TDGF from sensor 1 to sensor 2 in the positive time domain, while $G_{21}(-t)$ is the TDGF from sensor 2 to sensor 1 in the negative time domain, and $*$ refers to the convolution operator. Here, $Q(t)$ is a function that considers

the integrated effect of the source spectrum, the source distribution, the transducer characteristics, and the property of the medium, yet is independent of the positions of each N source excitations. In this dissertation, rather than its time derivative, the averaged NCF of Eq. (3.3) is used for damage detection. This is because a non-ideal environment is created by finite number of sources having not perfectly uniform distribution to simulate a realistic structure (Chehami et al., 2014).

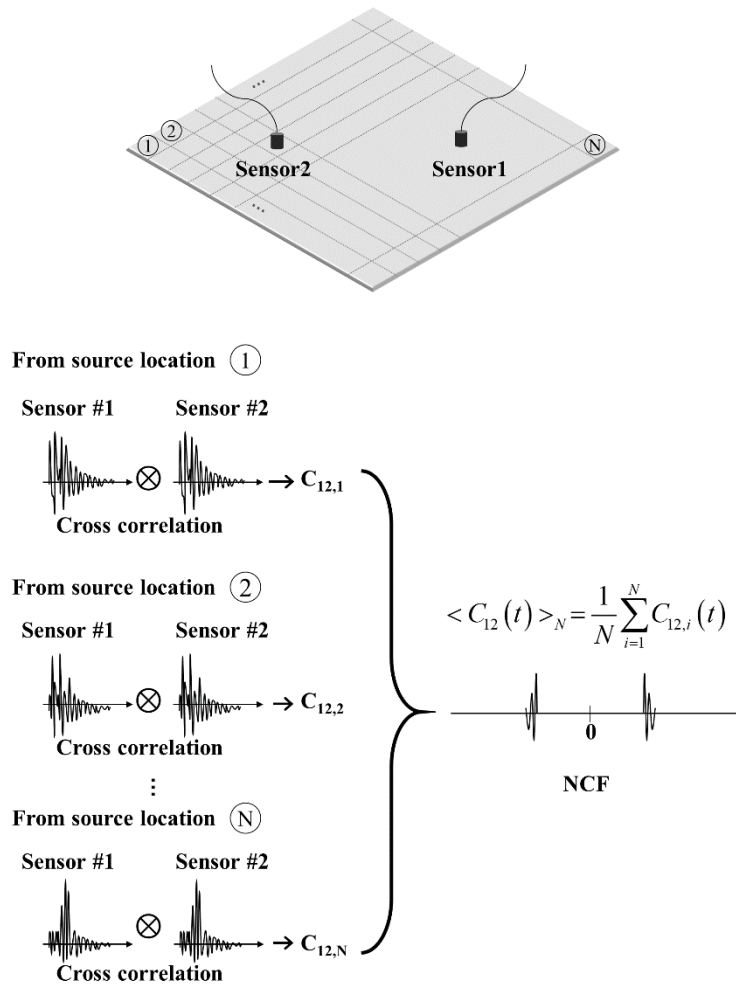


Figure 3-1: Extraction of the noise cross-correlation function (NCF) from ambient

vibrations. Separate N noise sources are used, denoted as circled text 1, 2, ... N to produce the diffuse field.

In practice, the averaged NCF is not a deterministic function. When the diffuse field is not fully generated due to an insufficient number of sources, the averaged NCF shows random fluctuations from the mean field. These fluctuations act as noise, interfering with the damage detection from the cross-correlation of the diffuse field. To compare the two extracted signals as a function of the number of sources, a metric defined as the cross-correlation coefficient at zero delay is given by (Tippmann and Lanza di Scalea, 2015)

$$Corr(0) = \frac{\int_{-\infty}^{\infty} \langle C_{12}(t) \rangle_{N_1} \langle C_{12}(t) \rangle_{N_2} dt}{\sqrt{\int_{-\infty}^{\infty} \langle C_{12}(t) \rangle_{N_1}^2 dt \int_{-\infty}^{\infty} \langle C_{12}(t) \rangle_{N_2}^2 dt}}, \quad (3.4)$$

where N_1 and N_2 are the number of sources selected randomly. Later, Eq. (3.4) will be used to evaluate the similarity of the two NCFs.

Statistics of the averaged NCF and feature vectors

The averaged NCF between two receivers provides path information which changes when the structure is damaged as waves reflect or scatter at the defect boundary. To quantify such distortions, statistics of the extracted field are considered in the time domain (Figueiredo et al., 2009). First, the averaged NCF is squared and normalized by its integral value in the positive time region, which is defined as

$$f(t) = \frac{\langle C_{12}(t) \rangle_N^2}{\int_0^{\infty} \langle C_{12}(t) \rangle_N^2 dt} \quad \text{in } t > 0. \quad \text{From the } f(t), \text{ a root-mean-square (RMS) index}$$

and a total of four statistical moments of mean, variance, skewness, and kurtosis are obtained. Then, the RMS index is defined as (Zill et al., 2006)

$$T_0 = \sqrt{\frac{1}{t_2 - t_1} \int_{t_1}^{t_2} f^2(t) dt}, \quad (3.5)$$

Similarly, the mean and variance are defined as $T_1 = E[t] = \int_0^{\infty} tf(t) dt$ and

$T_2 = E[(t - T_1)^2]$, respectively (Bendat and Piersol, 2011). Skewness and kurtosis

are given as follows: $T_n = E\left[\frac{(t - T_1)^n}{\sqrt{T_2}^n}\right]$, where n=3 and 4 indicate the skewness

and kurtosis, respectively (Gubner, 2006). Skewness can have positive or negative

values, whereby positive skewness indicates that more data are concentrated below

the mean, while negative skewness indicates that more data are distributed above the

mean. The kurtosis evaluates the quantity of data distributed in tails. In standard

normal distribution, the kurtosis value is 3. The distribution which has a kurtosis

greater than three has a higher peak and longer tail than the standard normal

distribution. On the contrary, a distribution with kurtosis less than three has a lower

peak and shorter tail than the standard normal distribution. These five indices

constitute a feature vector for damaged or undamaged cases, which are used as input

data of the damage-detection algorithm. These five statistics are listed in Table 3-1.

Table 3-1: Summary of each damage index (DI). $f(t)$ is defined as

$$\frac{(\langle C_{12}(t) \rangle_N)^2}{\int_0^\infty (\langle C_{12}(t) \rangle_N)^2 dt}$$

Damage index	Equation
Mean	$T_1 = E[t] = \int_0^\infty tf(t) dt$
Variance	$T_2 = E[(t - T_1)^2]$
Skewness	$E \left[\left(\frac{(t - T_1)}{\sqrt{T_2}} \right)^3 \right]$
Kurtosis	$E \left[\left(\frac{(t - T_1)}{\sqrt{T_2}} \right)^4 \right]$
RMS	$\sqrt{\frac{1}{t_2 - t_1} \int_{t_1}^{t_2} f^2(t) dt}$

3.3. Experiment and data processing

Experimental setup

The experiment is conducted on a square aluminum plate with a length of 40 cm and a thickness of 2 mm, as shown in Fig. 3-2. Two accelerometers B&K type 4383 measuring the out-of-plane accelerations of the plate are installed at $(x, y) = (27\text{cm}, 13\text{cm})$ and $(13\text{cm}, 27\text{cm})$ for the plane coordinate shown on the left side of Fig. 3-2, and are connected to the charge amplifier B&K NEXUS. 118 square grids are drawn on the plate and then a hand-held impulse hammer Dytran 5800B4 is struck at each grid to excite the plate. The impulse signal generated by the hammer

is not exactly the same at every excitation since it is conducted manually.

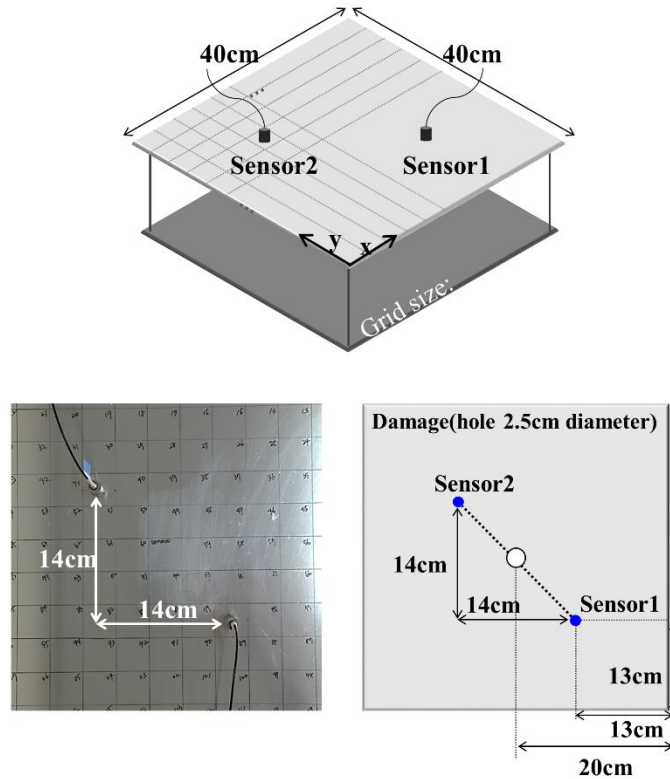


Figure 3-2: Experimental setup. Aluminum plate is 40 cm in width and length with a 2 mm-thickness. Two accelerometers are placed at $(x, y) = (27 \text{ cm}, 13 \text{ cm})$ and $(13 \text{ cm}, 27 \text{ cm})$ and damages are at the center of the plate.

Fig. 3-3 shows the histogram of a thousand zero-delay cross-correlation coefficients, each of which is calculated with two impulses randomly sampled from the total impulses of 472 used for the experiment, and computed by Eq. (3.4) in which $\langle C_{12}(t) \rangle_{N_1}$ and $\langle C_{12}(t) \rangle_{N_2}$ are replaced by the hammer impulses. Here, those hammer impulses are records of impulses at the moment of hammering acquired by the hammer's own sensor. In Fig. 3-3, it is shown that most of the values are over

0.6 and the mode is 0.76. Fig. 3-4 represents a typical hammer impulse spectrum acquired from the impulse hammer (black solid line) and the noise spectrum in case of no excitation (blue dotted line). The energy of the impulse dominates below 2 kHz and is distinguishable from the background noise up to the frequency range of 7 kHz.

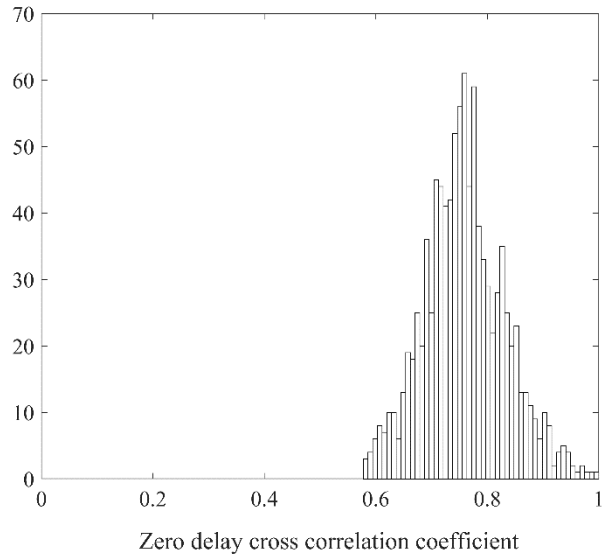


Figure 3-3: Histogram of a thousand zero-delay cross-correlation coefficient

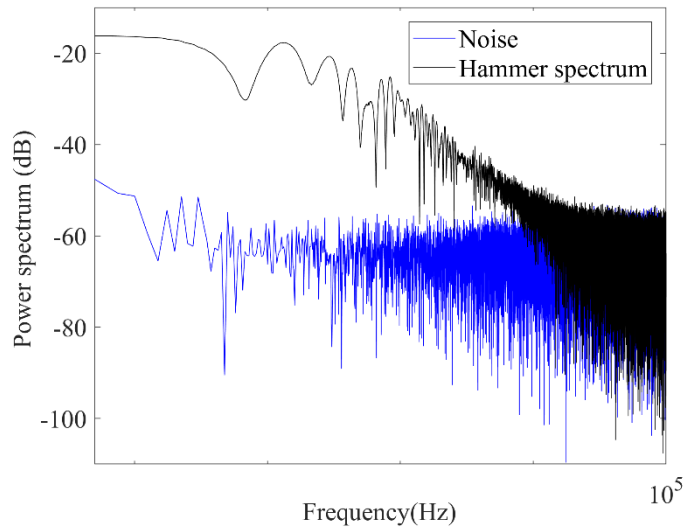


Figure 3-4: Typical spectrum of an impulse hammer excitation. The black solid line presents the spectrum from the impulse hammer and the blue dotted line is the noise spectrum in case of no excitation. Most of the impulse energy is distributed below 7 kHz.

As described in the introduction, two damage scenarios are tested in the experiment. One damage scenario is a 25 mm diameter punctured hole located at the center of the plate, while the other is an attached square clay with a length of 25 mm and a thickness of 10 mm. For these two damaged conditions and corresponding undamaged conditions, four experiments were carried out. Two experiments for the attached-clay case are performed in a complete square plate with or without the attached square clay. In the case of the punctuated-hole, two plates of one complete square plate and one square plate with a punctuated hole are respectively used for undamaged and damaged scenarios. We mention that two plates used in the punctuated-hole case have the same size and material property except that one of two has a punctuated hole; consequently, 472 (118 grid points excitation \times 4) time

signals are collected at each accelerometer for each scenario. The measured data are processed by MATLAB software. The configuration of the experiment is depicted in Fig. 3-5.

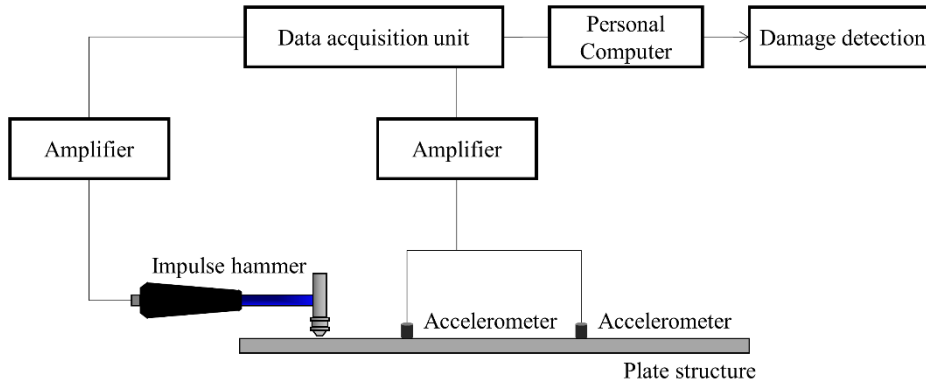


Figure 3-5: Experimental configuration.

Data processing

The sampling frequency is 200 kHz and the time segments to the first 0.5 seconds are taken for the data analysis. Using Eq. (3.2), the averaged NCF for N excitations is calculated after normalization of each cross-correlation function. Other normalization methods such as clipping and one-bit normalization that are directly applied to the received time signal, are not used for the analysis. Although such techniques slightly increase the SNR of the coherent fields, its benefit in damage detection is small in comparison with the increased additional processing costs. Fig. 3-6 shows an averaged NCF for 118 excitations for the undamaged plate. For a fully diffused field, the averaged NCF is symmetric in time, while the TDGF is an antisymmetric function. In Fig. 3-6, the zero-delay cross-correlation coefficient of the flipped left part and right part of the averaged NCF is 0.994. Fig. 3-7 plots the

zero-delay cross-correlation coefficient between the averaged NCFs for the N and 118 excitations. The N sources are randomly chosen among a total of 118 sources for a trial ($N = 1 \sim 117$); in other words, N_1 is 118 and N_2 is varied from 1 to 117 in Eq. (3.4). For each N , 100 trials are conducted. In Fig. 3-7(a), larger dispersion is observed as the number of sources is less than 10. This is because the reduced number of sources is insufficient to generate the diffuse field, coincident with several previous studies (Duroux et al., 2010; Weaver and Lobkis, 2005). Fig. 3-7(b) shows the mean curve of the cross-correlation coefficients. It is verified that the mean value rapidly converges to 1 as N increases.

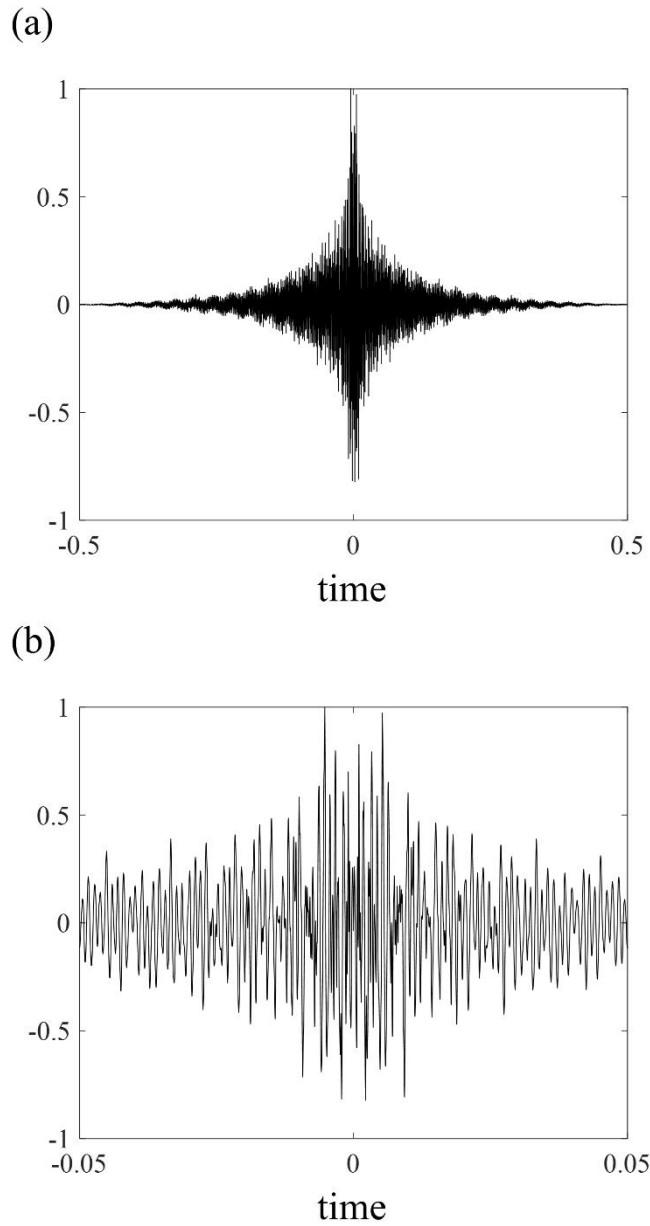


Figure 3-6: (a) NCF for 118 excitations of the undamaged plate. The averaged NCF is symmetric in time for fully diffuse field. The zero-delay cross-correlation coefficient of the left and right parts of the averaged NCF is 0.994. (b) Blow up of (a) for [-0.05 0.05].

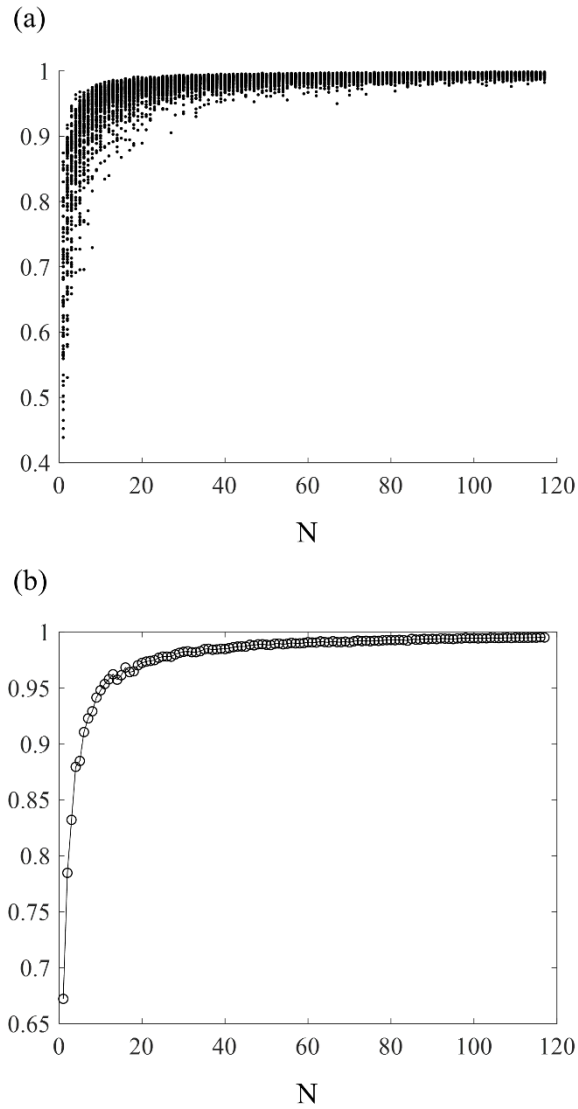


Figure 3-7: Zero-delay cross-correlation coefficients between the averaged NCFs of N and 118 excitations as a function of N . The N sources are randomly chosen among a total of 118 sources. A total of one hundred trials are conducted in (a) and larger fluctuations are shown in the small number of sources. (b) Mean curve of coefficients according to N .

3.4. Damage detection

Statistics of the averaged NCF by the damage type and the number of sources

To explore the characteristics of the five features listed in Table 3-1, the experimental data are examined for the damage type and the number of sources. Assuming that the N sources are excited on a plate, 1,000 sets of source locations are randomly sampled and applied to evaluate the averaged NCF for each of the undamaged, clay-attached, and hole-punctuated plates. The statistics are computed using the formulas given in Table 3-1 for the time interval of $[0, 0.5]$.

Fig. 3-8 represents a plot of the expected value of 1,000 samples of statistics as a function of the number of sources. The lines with circle, star, and square markers represent the undamaged plate, the hole-punctuated plate, and the clay-attached plate, respectively. As the number of sources increases, all statistics show a trend of converging to a constant value because a more stable NCF is generated in the more diffuse field with large sources. It is interesting that most of the features are distinguishable from each other for small N . In Fig. 3-8, the mean and variance of the hole-punctuated plate are smaller than those of the undamaged and clay-attached plate; this is related to the shape of $f(t)$. In the hole-punctuated plate, most of the wave energy is concentrated on the early arrivals because of reflections at the hole boundary. On the contrary, early arrivals in the clay-attached plate undergo damping due to the clay, so the shape of $f(t)$ becomes flatter. This explains the small mean and variance of the hole-punctuated plate. Similar trends can be observed in the skewness and kurtosis. Since the $f(t)$ of the hole-punctuated plate has focused energy on the early arrivals, the skewness, kurtosis, and RMS are highest among the three cases. On the other hand, the skewness and kurtosis of the clay-attached plate

are the lowest. The RMSs of the clay-attached plate and undamaged plate are slightly distinguishable, but the former is higher than the latter. This difference is the consequence of the area normalization applied to the averaged NCF.

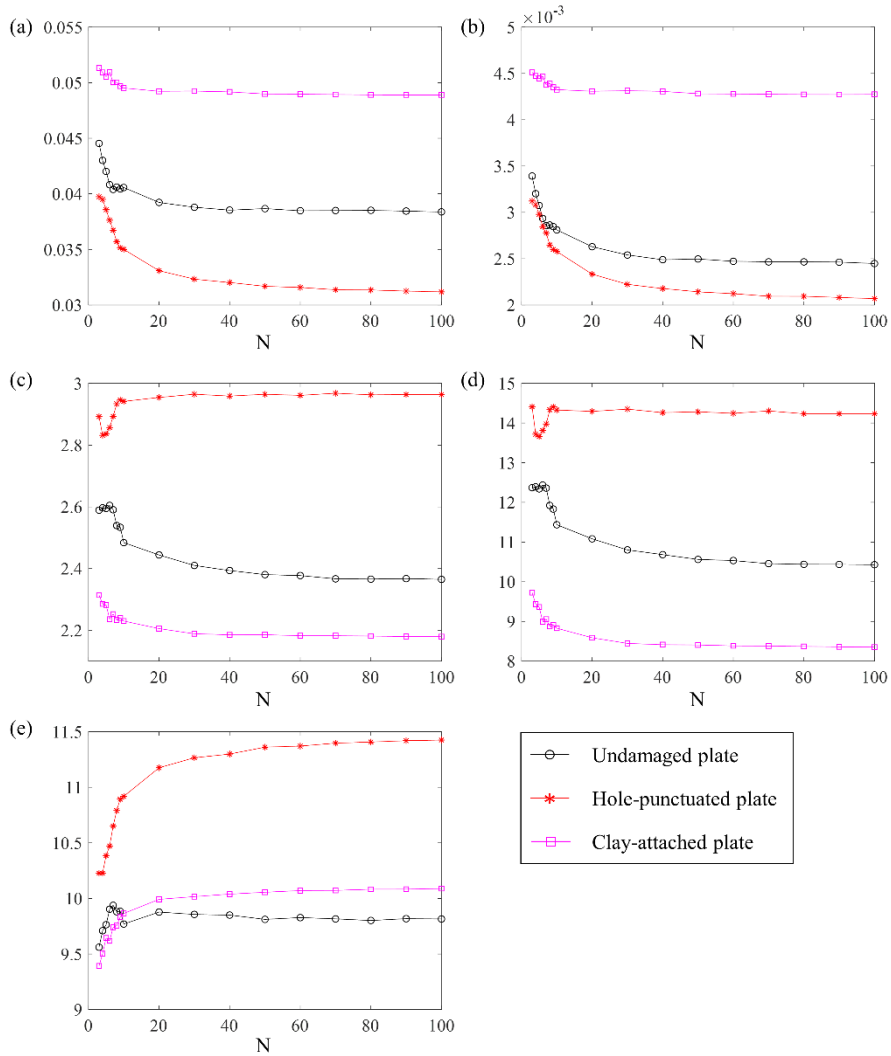


Figure 3-8: Mean of each damage index distribution. (a) Mean, (b) variance, (c) skewness, (d) kurtosis, (e) RMS according to N .

Fig. 3-9 plots the $f(t)$ and its cumulative distribution function (CDF) of the undamaged plate (black solid line), the hole-punctuated plate (red dash-dot line), and the clay-attached plate (magenta dashed line) for the 118 sources. In Fig. 3-9(b), it is clear that the hole-punctuated plate shows more energy concentrations on the early arrivals.

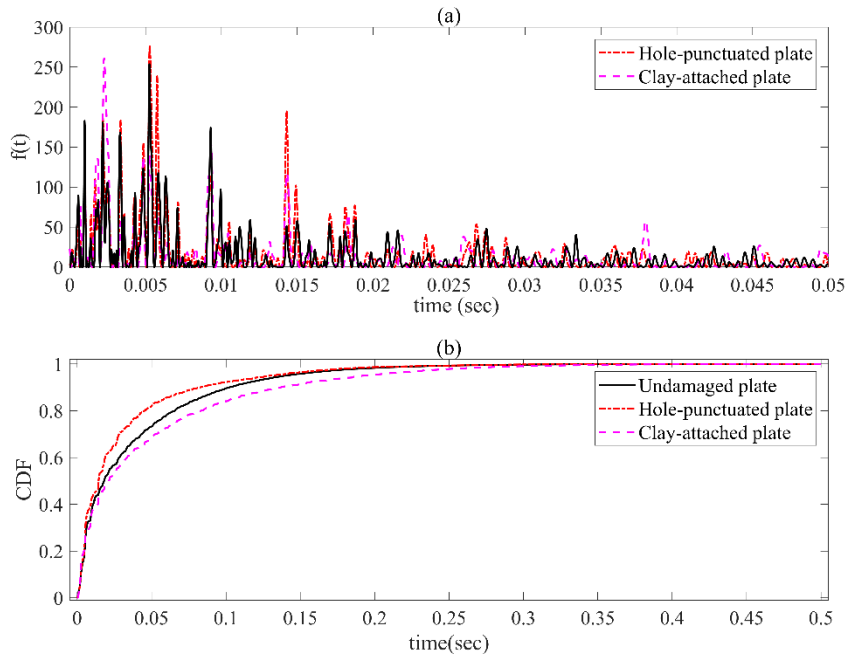


Figure 3-9: (a) The normalized NCF defined as $f(t) = \frac{(\langle C_{12}(t) \rangle_{118})^2}{\int_0^\infty (\langle C_{12}(t) \rangle_{118})^2 dt}$, (b) the

CDF of $f(t)$. The black solid line presents the undamaged plate, and the red dash-dot line is for the hole-punctuated plate, and the magenta dashed line indicates the clay-attached plate for both in (a) and (b).

Figs. 3-10 and 3-11 plot the histograms of 1,000 samples, comparing the undamaged and hole-punctuated plates where N is 100 in Fig. 3-10 and 50 in Fig. 3-

11. The white histograms with black lines are obtained from the undamaged plate, while the red histograms are obtained from the hole-punctuated plate. The histograms of the mean and variance for the undamaged plate are on the right side of those for the hole-punctuated plate, and histograms of the other three statistics for the intact condition are on the left side of those for the hole-punctuated plate. Figs. 3-12 and 3-13 compare the histograms of the undamaged plate (white histograms) and the clay-attached plate (red histograms), where N is 100 in Fig. 3-12 and 50 in Fig. 3-13. Contrary to Figs. 3-10 and 3-11, the histograms of mean and variance for the undamaged plate are on the left side of those for the clay-attached plate, while the histograms of skewness and kurtosis for the intact plate are on the right side of those for the clay-attached plate. Figs. 3-10 ~ 3-13 demonstrate that the histograms of the undamaged and damaged plate become more separate for a larger number of sources which generate a more accurate NCF.

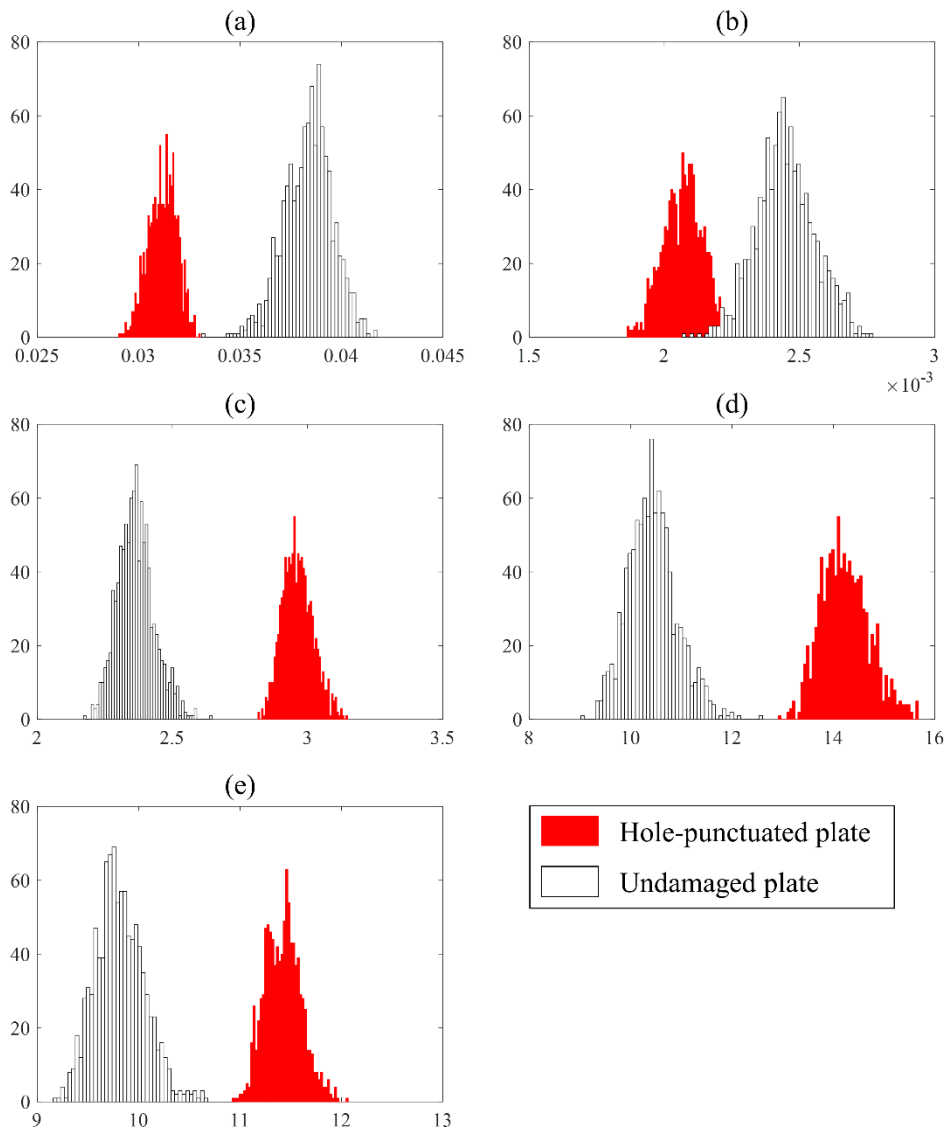


Figure 3-10: Histogram of each damage index. (a) Mean, (b) variance, (c) skewness, (d) kurtosis, (e) RMS of the undamaged plate (white histograms) and the hole punctuated plate (red histograms) for $N=100$.

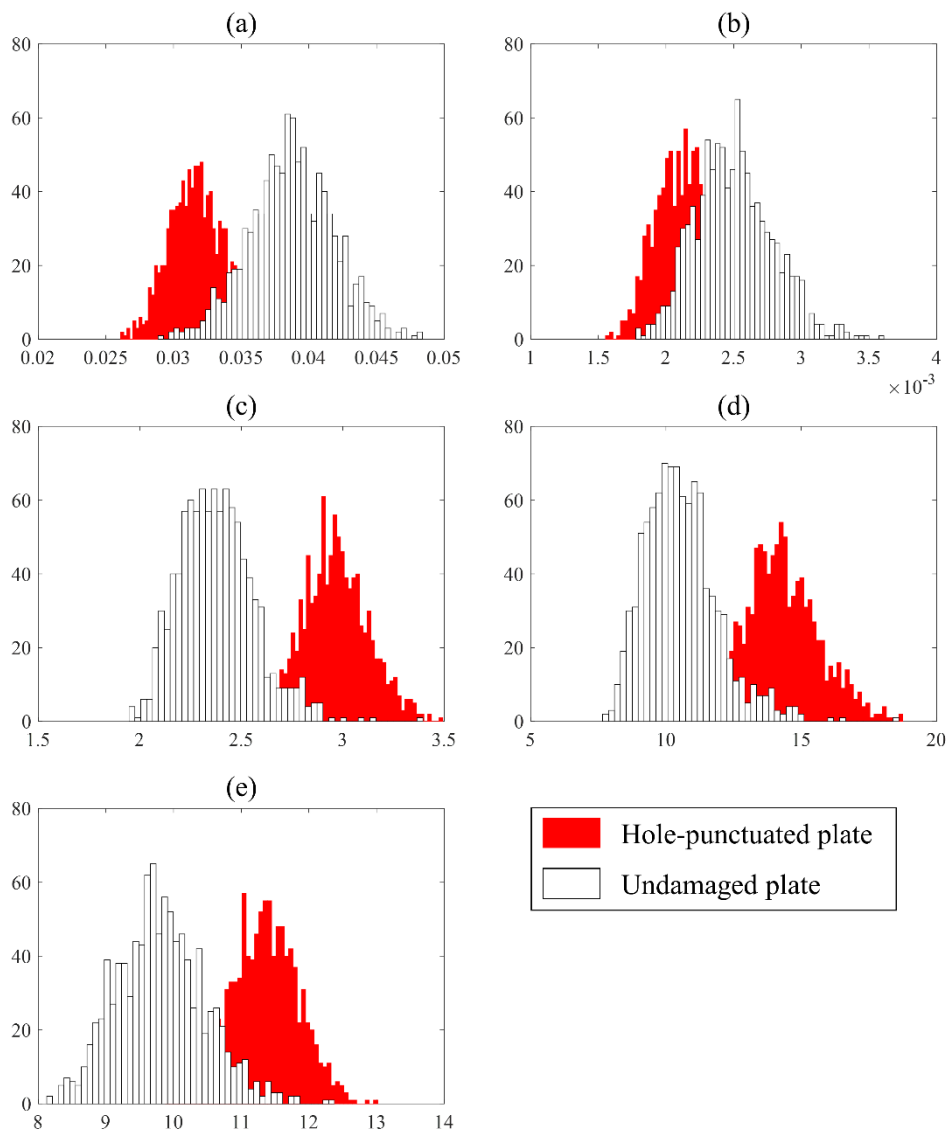


Figure 3-11: Histogram of each damage index. (a) Mean, (b) variance, (c) skewness, (d) kurtosis, (e) RMS of the undamaged plate (white histograms) and the hole punctuated plate (red histograms) for $N=50$.

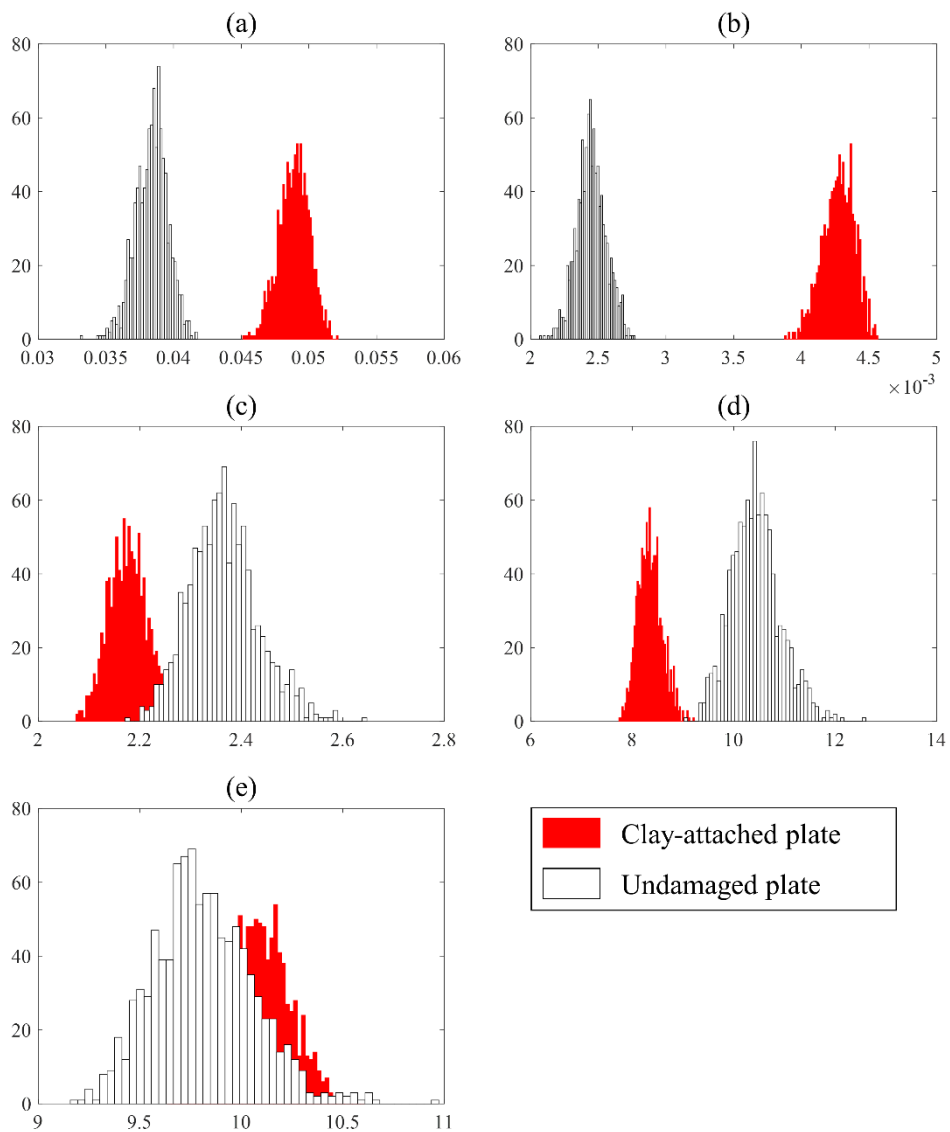


Figure 3-12: Histogram of each damage index. (a) Mean, (b) variance, (c) skewness, (d) kurtosis, (e) RMS of the undamaged plate (white histograms) and the clay attached plate (red histograms) for $N=100$.

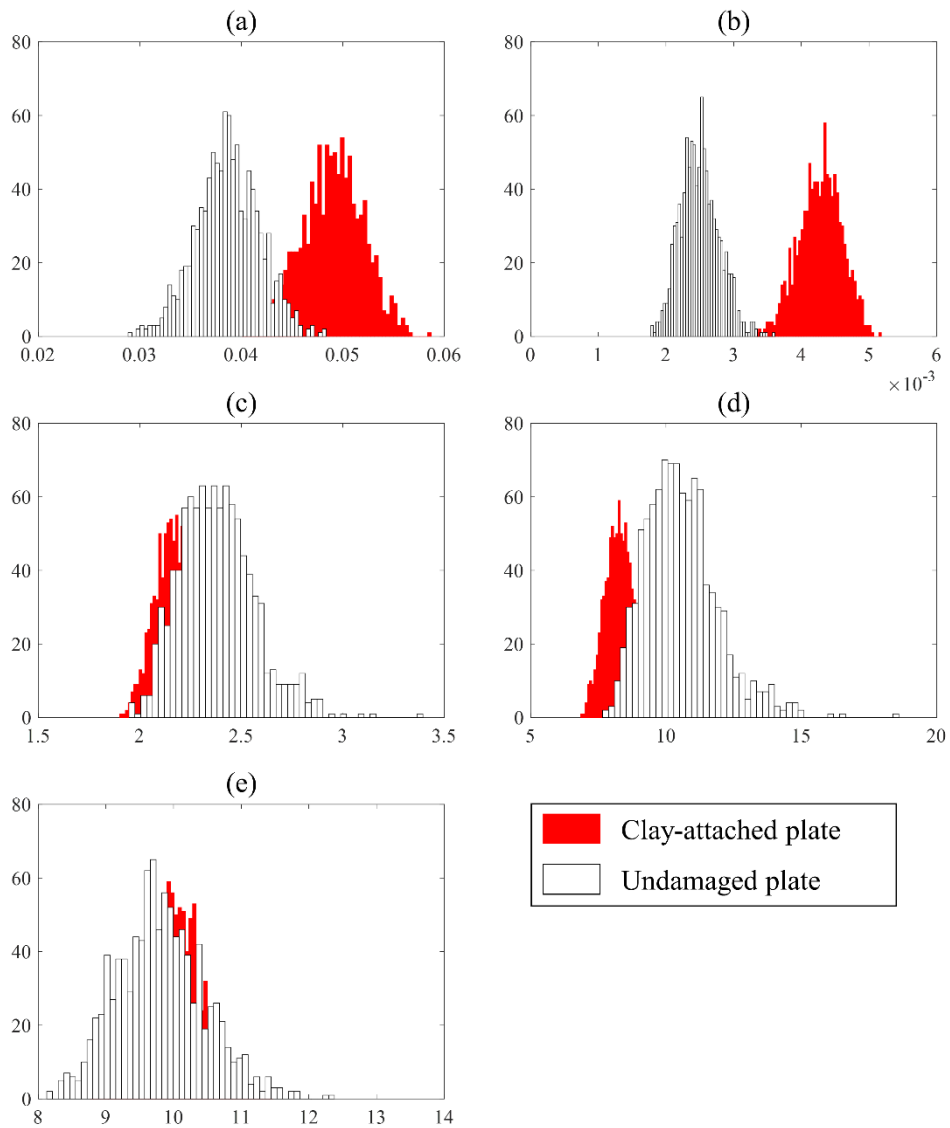


Figure 3-13: Histogram of each damage index. (a) Mean, (b) variance, (c) skewness, (d) kurtosis, (e) RMS of the undamaged plate (white histograms) and the clay attached plate (red histograms) for $N=50$.

Damage classification using support vector machine

For damage classification with five statistics, denoted by the damage index (DI) in this study, the simple linear support vector machine (SVM) was performed. For each number of sources and type of damage, the SVM is operated on 2,000 DI samples, half of which are calculated from the undamaged plate and the rest are calculated from the damaged plate. One DI sample is generated with the N sources chosen randomly from the 118 exciting noise sources for each plate. DI samples are partitioned into the training data (1,600 samples) for learning, validation data (200 samples) to decide the parameter of the classifier, and test data (200 samples) to adequately assess the performance of the classifier adequately. The parameter of the SVM is determined by comparing the validation set error, and the test error is analyzed in the test data using the established classifier from the validation set.

Before using the SVM, the principal component analysis (PCA) is applied on the training data for data visualization as well as for classification. The PCA is a statistical process which searches new axes on principal components (PC) that represent the original data appropriately. Firstly, the PCA computes the first PC having the largest variance, which minimizes the sum of the squared error between the original data and the projected data on to the PC. Next, the PCA finds the second PC orthogonal to the first PC with the second largest variance, and the subsequent PCs are analyzed in the same way (Morrison et al., 1998). All PCs are searched using the singular value decomposition (SVD), where the eigenvectors correspond to PCs. The first PC has the largest eigenvalue and the following PCs have succeeding largest eigenvalues. To reduce the dimension of the data, the number of PCs is determined considering the cumulative percentage of total variation, t_m (Jolliffe, 2002) of Eq. (2.4). The t_m indicates the number of m largest PCs that can explain the total

variation of the original data and is defined by the user's desire such as 80% or 90%. In this study, the t_m is decided as 90%, and the corresponding m is 2. Accordingly, the original training set, composed of 1,600 samples of five-dimensional (5-D) space, are projected to the two-dimensional (2-D) space constructed from the first two PCs. The SVM is applied to these projected training data to learn the linear classifier. Additional classification results using five-dimensional data are presented in appendix A.1.

The SVM is a binary classifier which maximizes the margin defined as the smallest distance between the decision line and any of the data (Bishop, 2006). The SVM produces sparse solutions which can make predictions using a subset of the training data known as support vectors. In this study, the linear decision line was computed as the data were separable. And the box constraint C of the linear decision line was calculated by analyzing the validation data (Bottou et al., 2007). The box constraint C can control the strictness of separation; for example, if C increases, it allows fewer support vectors with stricter separation. The box constraint is tested on 11 values $[1, 10, \dots, 100]$, and is determined to minimize the validation error. To calculate the validation error, the validation set needs to be projected onto the same 2-D space generated in the training set, and the error is then computed using the linear hyperplane learned from the projected training data. For each 10 cases of the number of sources $N = [10, 20, \dots, 100]$, the box constraint is estimated as $C = [1, 1, 100, 100, 1, 1, 100, 100, 100, 100]$ for the hole-punctuated plate and as $C = [1, 100, 100, 100, 100, 100, 100, 100, 100, 100]$ for the clay-attached plate. Using these box constraints, the linear decision line can be determined.

Third, the test data projected onto the same PCs of the training data are examined to evaluate the performance of the constructed classifier. Fig. 3-14 plots

the projected data comparing the undamaged and hole-punctuated plates, where the number of sources is 5, 50, and 100. Fig. 3-15 compares the projected data of the undamaged and clay-attached plate, while the other plot settings are the same as those in Fig. 3-14. In both Figs. 3-14 and 3-15, the x-axis is the first PC, while the y-axis is the second PC. The left plot represents the projected training data and the right plot shows projected test data in each subplot. In the figure, the circle and square markers represent the undamaged plate, and the cross and star markers correspond to the damaged plate. As the distance of histograms between the undamaged and damaged plate increases for the increased number of sources in the original data, the projected data are naturally also more separate for an increased number of sources. When the number of sources is smaller than 10, the data are nearly non-separable as the field is not diffuse enough to make a clear difference between the undamaged and damaged conditions, as shown in Figs. 3-14(a) and 3-15(a). If the number of sources is over 50, the data between the undamaged and damaged plate for both damage types become almost distinguishable, as shown in Figs. 3-14(c) and 3-15(c). Interestingly, when the number of sources is 50 as shown in Fig. 3-15(b), the data for the clay-attached case are more separate than the hole-punctuated case in Fig. 3-14(b). This is because the damage by clay attachment is more sensitive in this study because of its nonlinear behavior.

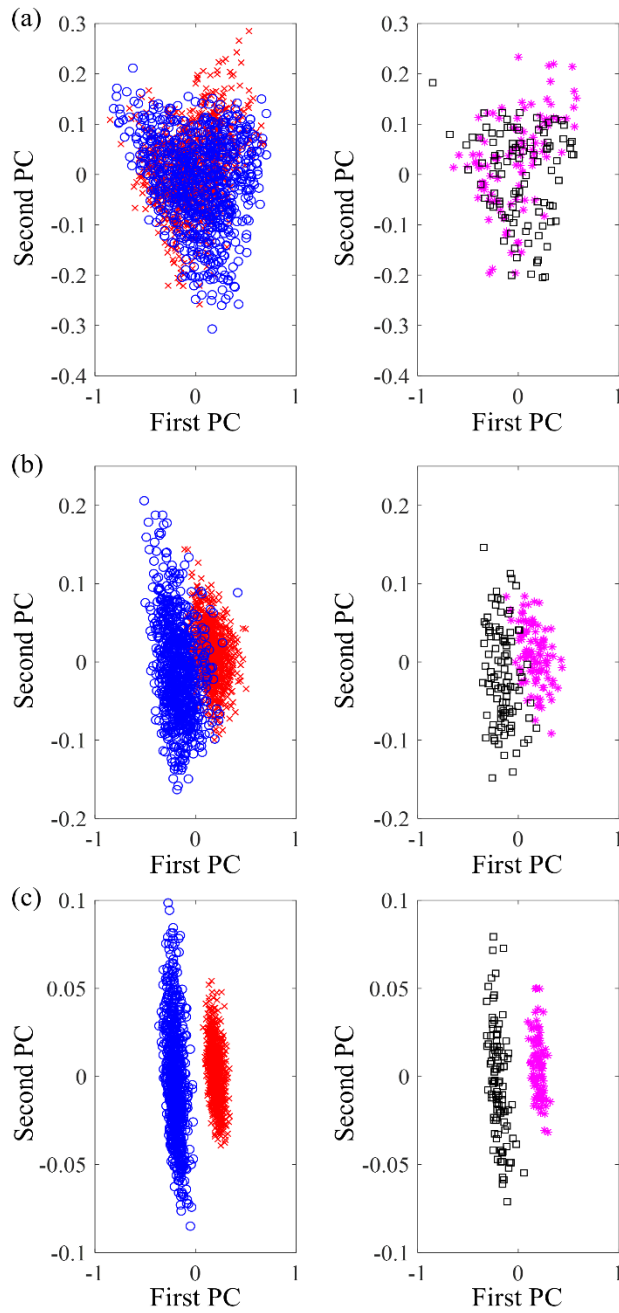


Figure 3-14: Data projected to first and second principal components in the undamaged and hole punctuated plate. The left plots show training data and the right plots represents test data in (a)-(c). The number of source N is 5, 50, and 100 for (a), (b), and (c), respectively. The circle and square markers show undamaged

plates while the cross and star markers show damaged state (punctuated-hole).

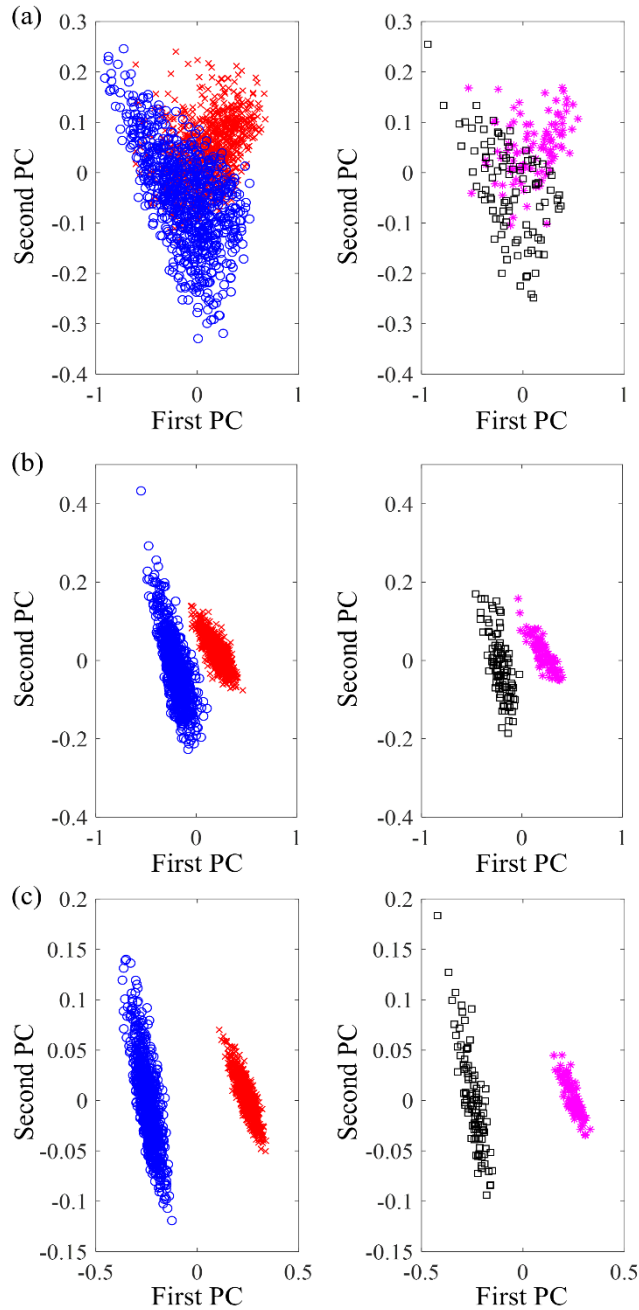


Figure 3-15: Data projected to first and second principal components in the undamaged and clay attached plate. The left plots show training data and the right plots represent test data in (a)-(c). The number of source N is 5, 50, and 100 for (a),

(b) and (c), respectively. The circle and square markers show undamaged plates, while the cross and star markers show damaged state (clay-attached).

Fig. 3-16 shows the classification result for 50 sources for the hole-punctuated plate and the clay-attached plate. In each subplot, the left plot displays projected training data and the right plot represents projected test data. The black line represents the decision line generated from the training data, the triangle markers in the projected test data represent misclassified data such as test errors, and other markers are same as those of Fig. 3-15. The test errors can be divided into two groups: type 1 and type 2 errors which represent a false alarm and a miss, respectively (Fassois and Sakellariou, 2007). In the projected test plots in Fig. 3-16(a), the errors (triangle markers) on the right side of the decision line correspond to type 1 errors, while the errors on the left side of the hyper plane correspond to type 2 errors. In Fig. 3-16(b) for the clay-attached plate, no misclassified data appear because the projected data are perfectly separate, which again signifies larger change of waveform in the clay-attached plate.

Finally, the classification results according to the number of sources are presented in Fig. 3-17 and Table 3-2. The figure displays the averaged accuracy for the hole-punctuated plate (blue dashed line) and the clay-attached plate (blue solid line). When the number of sources is less than 70, the accuracy for the clay-attached plate tends to be higher than that of the hole-punctuated plate. Hence, the accuracy for the clay-attached plate is generally higher than that for the hole-punctuated plate. This is because the features of the mean and variance in the clay-attached plate are clearly distinct from those of the undamaged plate, as shown in Figs. 3-12 and 3-13. In both damage types, the accuracy increases monotonically according to the increment of the number of sources, since an accurate NCF can be achieved in a

more diffuse field, which eventually generates more distinct data between the damaged and undamaged plate. The detailed values or accuracies, type 1 error, and type 2 error are presented in Table 3-2.

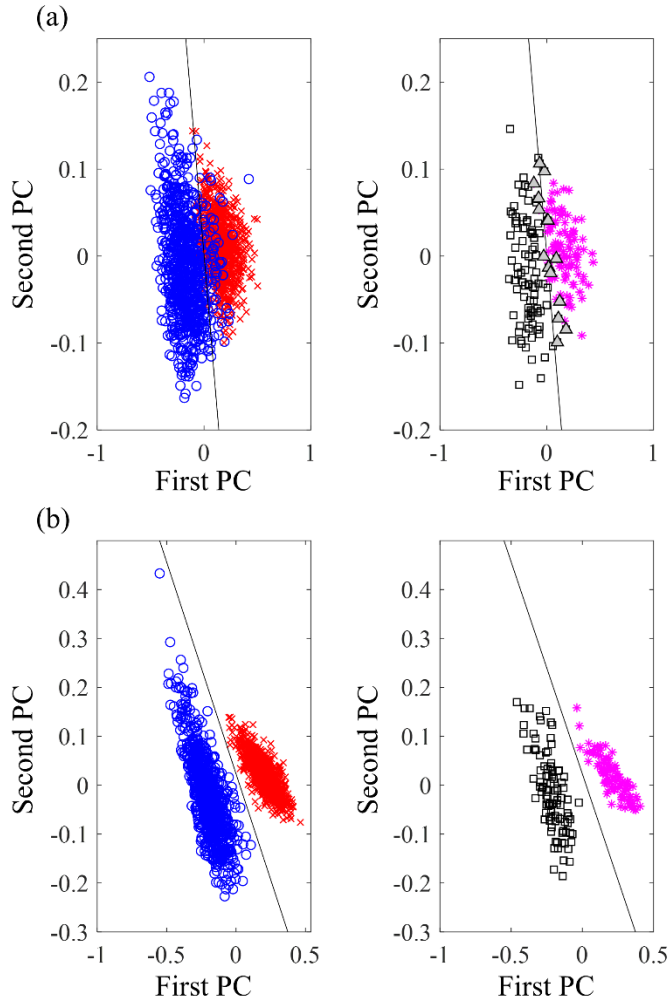


Figure 3-16: Result of SVM in projected data of $N=50$, (a) for the hole-punctuated case where the data are same with those of in Fig. 3-14(b), and (b) for the clay-attached case where the data are same with those of in Fig. 3-15 (b). The left plots show training data and the right plots represent test data in both (a) and (b). The circle and square markers express the undamaged plate, while the cross and star markers present the damaged state. The solid black line represents the linear

hyperplane and the triangle markers with gray face color indicate the test errors.

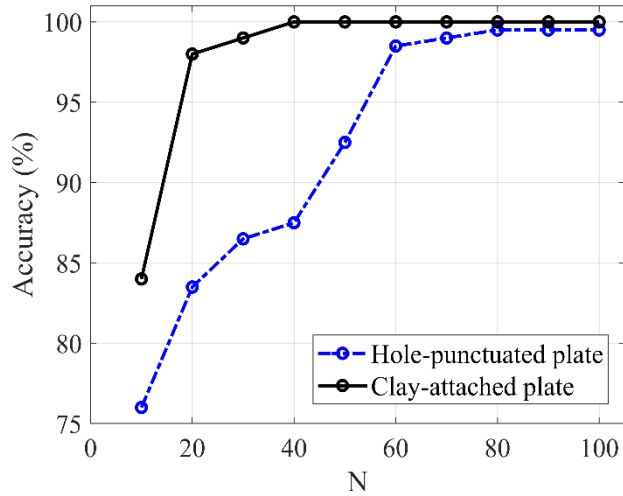


Figure 3-17: Averaged accuracy according to the number of sources. The blue dashed line presents the hole-punctuated plate, while the black solid line indicates the clay-attached plate.

Table 3-2: Binary classification results of the SVM.

	N									
	10	20	30	40	50	60	70	80	90	100
Hole punctuated plate										
Type 1 error (%)	26	18	18	16	11	3	1	1	1	1
Type 2 error (%)	22	15	9	9	4	0	1	0	0	0
Averaged error (%)	24	16.5	13.5	12.5	7.5	1.5	1	0.5	0.5	0.5
Averaged accuracy (%)	76	83.5	86.5	87.5	92.5	98.5	99	99.5	99.5	99.5
Clay attached plate										
Type 1 error (%)	15	1	0	0	0	0	0	0	0	0
Type 2 error (%)	17	3	2	0	0	0	0	0	0	0
Averaged error (%)	16	2	1	0	0	0	0	0	0	0
Averaged accuracy (%)	84	98	99	100	100	100	100	100	100	100

3.5. Summary and conclusions

In this chapter, a damage detection algorithm using diffuse elastic fields is proposed. This algorithm has three stages. First, the averaged NCF for each of the undamaged, hole-punctuated, and clay-attached plates is computed from the two-point cross-correlation of diffuse acceleration fields, which are generated by random excitations of the plate. Second, the time-domain statistics of mean, variance, skewness, kurtosis, and RMS values are extracted from the obtained NCF, consisting of feature vectors for damage detection. For redundancy reduction, the 5-D vector is projected onto two principal components using PCA, considering the cumulative percentage of total variations is 90%. Finally, the linear SVM is used for damage detection. The linear hyperplane is learned from the projected training set, and the parameters of the classifier that minimize the validation set error are determined.

The proposed algorithm is applied to the experimental data acquired in the aluminum plate. Our classifier shows good performance in both damaged cases, but is slightly more sensitive to the clay-attached case. This is because the decaying of early paths by the clay has more influence on the shape of NCF than the scattered paths created by the hole. In the fully diffuse field with large N , the data sets of the undamaged and damaged plates are perfectly separable in both cases of punctuated hole and clay attachments. Although its performance is degenerated in a less diffuse field, the error is not high, even for small N . This implies that the error resulting from the incomplete construction of the averaged NCF can be mitigated by the ability of the classifier. Therefore, the use of a more intellectual classifier may further improve the detection performance and reduce the cost of the monitoring system using the diffuse field.

In this study, damages of the punctuated hole and attached clay are investigated, while crack-like damage is not tested. Although we cannot assure how much NCF variation will be induced by the crack, the reflected paths at the crack boundary and its nonlinear behavior such as opening-and-closing called as clapping (Farrar and Worden, 2012) could change the NCF. And if any evidences of crack are observed in the NCF, the classifier could detect the damage. Meanwhile, the damage is located between two accelerometers and the effect of different location of sensor is not considered in this study. If the damage is developed at different location, the reflected paths will be changed which result in different distribution of damage indices from this study, while the detection performance would be dependent on the distance from the sensor pair to the damage. Researches about optimal placement of sensors for damage detection have been studied using population based techniques (Guo et al., 2004; Gao and Rose, 2006; Liu et al., 2008). Although searching optimal location of sensors is out of the scope of this study, further studies integrated with optimal sensor locations would be required for application to real environment.

3.6. Acknowledgement

This chapter is a revised material of Ocean Engineering, 2018, with authors S. Jung, W. Seong, and K. Lee. Reprinted with permission from S. Jung, W. Seong, and K. Lee, "Damage detection on an aluminum plate from the cross-correlation of diffuse field using the support vector machine," Ocean. Eng. 161, 88–97 (2018). Copyright 2018, Ocean Engineering.

Bibliography

- Bendat, J.S., Piersol, A.G., 2011. Random data: analysis and measurement procedures, John Wiley & Sons.
- Bishop, C., 2006. Pattern recognition and machine learning. Springer-Verlag New York.
- Bottou, L., Chapelle, O., DeCoste, D., Weston, J., 2007. Large-scale kernel machines, MIT press.
- Chehami, L., Moulin, E., De Rosny, J., Prada, C., Bou Matar, O., Benmeddour, F., Assaad, J., 2014. Detection and localization of a defect in a reverberant plate using acoustic field correlation. *J. Appl. Phys.* 115 (10), 104901.
- Davis, P., Brockhurst, J., 2015. Subsea pipeline infrastructure monitoring: a framework for technology review and selection. *Ocean Eng.* 104, 540–548.
- Duroux, A., Sabra, K.G., Ayers, J., Ruzzene, M., 2010. Extracting guided waves from cross-correlations of elastic diffuse fields: Applications to remote structural health monitoring. *J. Acoust. Soc. Am.* 127 (1), 204–215.
- Farrar, C.R., Worden, K., 2007. An introduction to structural health monitoring. *Philos. Trans. R. Soc. A Math. Phys. Eng. Sci.* 365, 303–315.

- Farrar, C. R., Worden, K., 2012. Structural health monitoring: a machine learning perspective. John Wiley & Sons.
- Fassois, S.D., Sakellariou, J.S., 2007. Time-series methods for fault detection and identification in vibrating structures. *Philos. Trans. R. Soc. A Math. Phys. Eng. Sci.* 365, 411–448.
- Figueiredo, E., Park, G., Figueiras, J., Farrar, C., Worden, K., 2009. Structural health monitoring algorithm comparisons using standard data sets. *Los Alamos Natl. Lab. LA-14393 6*.
- Gao, H., Rose, J. L., 2006. Ultrasonic sensor placement optimization in structural health monitoring using evolutionary strategy. In: *AIP Conference Proceedings*.
- Gubner, J.A., 2006. *Probability and random processes for electrical and computer engineers*, Cambridge University Press.
- Guo, H. Y., Zhang, L., Zhang, L. L., Zhou, J. X., 2004. Optimal placement of sensors for structural health monitoring using improved genetic algorithms. *Smart materials and structures*, 13 (3), 528–534.
- Jamalkia, A., Ettefagh, M.M., Mojtahedi, A., 2016. Damage detection of TLP and spar floating wind turbine using dynamic response of the structure. *Ocean Eng.* 125, 191–202.

- Jolliffe, I.T., 2002. *Principal component analysis*, John Wiley & Sons, Ltd.,
- Liu, W., Gao, W. C., Sun, Y., Xu, M. J., 2008. Optimal sensor placement for spatial lattice structure based on genetic algorithms. *Journal of Sound and Vibration*, 317 (1-2), 175-189.
- Liu, G., Zhai, Y., Leng, D., Tian, X., Mu, W., 2017. Research on structural damage detection of offshore platforms based on grouping modal strain energy. *Ocean Eng.* 140, 43–49.
- Lobkis, O.I., Weaver, R.L., 2001. On the emergence of the Green's function in the correlations of a diffuse field. *J. Acoust. Soc. Am.* 110 (6), 3011–3017.
- Morrison, D.F., 1998. *Multivariate analysis, overview*, John Wiley & Sons, Ltd.
- Roux, P., Kuperman, W.A., 2004. Extracting coherent wave fronts from acoustic ambient noise in the ocean. *J. Acoust. Soc. Am.* 116 (4), 1995–2003.
- Roux, P., Sabra, K.G., Kuperman, W.A., Roux, A., 2005. Ambient noise cross correlation in free space: theoretical approach. *J. Acoust. Soc. Am.* 117 (1), 79–84.
- Sabra, K.G., Roux, P., Kuperman, W.A., 2005. Arrival-time structure of the time-averaged ambient noise cross-correlation function in an oceanic waveguide. *J. Acoust. Soc. Am.* 117 (1), 164–174.

- Sabra, K.G., Srivastava, A., Lanza di Scalea, F., Bartoli, I., Rizzo, P., Conti, S., 2008. Structural health monitoring by extraction of coherent guided waves from diffuse fields. *J. Acoust. Soc. Am.* 123 (1), EL8-EL13.
- Sabra, K.G., Winkel, E.S., Bourgoyne, D. a, Elbing, B.R., Ceccio, S.L., Perlin, M., Dowling, D.R., 2007. Using cross correlations of turbulent flow-induced ambient vibrations to estimate the structural impulse response. Application to structural health monitoring. *J. Acoust. Soc. Am.* 121 (4), 1987–1995.
- Snieder, R., 2002. Coda wave interferometry for estimating nonlinear behavior in seismic velocity. *Science.* 295, 2253–2255.
- Sohn, B.H., Park, H.W., Law, K.H., Farrar, C.R., 2004. Damage detection in composite plates by using an enhanced time reversal method 20 (3), 141–151.
- Tippmann, J., Zhu, X., Scalea, F., 2014. Probabilistic structural health monitoring using passive-only damage detection by reciprocity of Green's function reconstructed from diffuse acoustic fields. In: *EWSHM-7th European Workshop on Structural Health Monitoring.*
- Tippmann, J.D., Lanza di Scalea, F., 2015. Passive-only damage detection by reciprocity of Green's functions reconstructed from diffuse acoustic fields with application to wind turbine blades. *J. Intell. Mater. Syst. Struct.* 26 (10), 1251–1258.

- Wapenaar, K., 2004. Retrieving the elastodynamic Green's function of an arbitrary inhomogeneous medium by cross correlation. *Phys. Rev. Lett.* 93, 254301.
- Weaver, R.L., Lobkis, O.I., 2005. The mean and variance of diffuse field correlations in finite bodies. *J. Acoust. Soc. Am.* 118 (6), 3447–3456.
- Weaver, R.L., Lobkis, O.I., 2004. Diffuse fields in open systems and the emergence of the Green's function (L). *J. Acoust. Soc. Am.* 116 (5), 2731–2734.
- Yi, J.-H., 2016. Laboratory tests on local damage detection for jacket-type offshore structures using optical FBG sensors based on statistical approaches. *Ocean Eng.* 124, 94–103.
- Zill, D.G., Wright, W.S., Cullen, M.R., 2006. *Advanced engineering mathematics*, Jones & Bartlett Learning.

Chapter 4

Severe slugging detection in the pipeline-riser system

Abstract

The use of accelerometer signals for early recognition of severe slugging is investigated in a pipeline-riser system conveying an air–water two-phase flow, where six accelerometers are installed from the bottom to the top of the riser. Twelve different environmental conditions are produced by changing water and gas superficial velocities, of which three conditions are stable states and the other conditions are related to severe slugging. For online recognition, simple parameters using statistics and linear prediction coefficients are employed to extract useful features. Binary classification to recognize stable flow and severe slugging is performed using a support vector machine. In multiclass classification, a neural network is adopted to identify four flow patterns of stable state, two types of severe slugging, and an irregular transition state between severe slugging and dual-frequency severe slugging. The performance is compared and analyzed according to the signal length for three cases of sensor location: six accelerometers, one accelerometer at the riser base, and one accelerometer at the top of the riser.

4.1. Introduction

Pipeline-riser structures composed of a production well, subsea pipeline, and vertical riser are generally used in offshore oil and gas fields. Mixtures of liquids, gases, and solid components are extracted from a reservoir, transported through a horizontal subsea pipeline of several kilometers, and raised to the topside via a vertical riser near the platform. In a pipeline-riser system, a more complicated multiphase flow can be developed than the flow from a simple horizontal or vertical pipe. In particular, a typical severe slugging can be generated in an undesired cycle with unstable blowout, causing large fluctuations in pressure that lead to structural damage and reduce the production rate (Schmidt et al., 1985; Yocum, 1973). In detail, the severe slugging can generate liquid overflow, high pressure in the separators, overload on the gas compressors, extra fatigue by repeated impact, increased corrosion, and low production (Hill et al., 1994; Kang et al., 1996; Pedersen et al., 2017; Sun and Jepson, 1992). In offshore pipeline facilities, stable operation is important for safety and economic benefits; therefore, unstable flow should be identified as quickly as possible.

Many studies have classified flow regimes using machine learning algorithms in simple horizontal, vertical pipe, or pipeline-riser systems (Blaney and Yeung, 2008; Goudinakis, 2004; Mi et al., 1998; Rosa et al., 2010; Trafalis et al., 2005; Wu et al., 2001; Ye and Guo, 2013; Zou et al., 2017). Wu et al. (2001) performed an experiment in a simple horizontal pipe using mixtures of mineral oil, air, and water to simulate oil–gas–water flow, and measured differential pressures. Features were extracted using the fractal dimension from denoised signals by the wavelet transform. A neural network (NN) was employed to classify stratified, intermittent, and annular

flows. Trafalis (2005) investigated flow recognition with a support vector machine (SVM) in a simple horizontal and a simple vertical pipe by applying gas and liquid superficial velocities and pipe diameter as features. Three regimes of bubble, intermittent, and annular flows were identified for the vertical flow, and four categories of annular, bubble, intermittent, and stratified flows were recognized for the horizontal flow. However, as superficial velocities are difficult to acquire in industrial pipelines, applying them to real industrial environments is not easy.

Meanwhile, in studies of the pipeline-riser systems, Goudinakis (2004) obtained differential pressures in an S-shaped riser system. The normalized differential pressures were used as inputs of the NN, where the length of sample was 100 s. Four classes of bubble, oscillation, slug, and severe slugging 1 were classified. Ye and Guo (2013) also conducted an experiment in an S-shaped riser and acquired differential pressure signals of 20-min length. Least-squares SVM (LS-SVM) classifiers were trained with features of statistical parameters such as absolute mean, variance, skewness, and power spectral densities. Severe slugging 1, severe slugging 2, severe slugging transition, oscillation, and stable flow were identified. Zou et al. (2017) measured the differential pressure in a pipeline-riser system. For fast recognition, they computed the mean and range of differential pressures as feature vectors for the LS-SVM. They analyzed the results for various signal lengths and, in particular, the shortest signals of 6.8 s were tested by the classifier trained using 8.99 s signals. Four classes of severe slugging, oscillation, stable like flow, and stable flow were recognized. In the case of a commonly used pressure gauge applied in the aforementioned studies, it is low-cost and usable at wide ranges of pressures and temperatures. However, it has some disadvantages: (1) a pressure tap can be blocked; (2) a pressure signal can be affected by either the water's or gas's velocity as well as

by the flow regime (Rosa et al., 2010); (3) it is difficult to move into another location once it is installed.

In addition to the previously mentioned measuring instrument, other devices have been used to identify the flow regime. Applications of electrical impedance measurements for flow regime recognition have been implemented by Hernández et al. (2006), Juliá et al. (2008), and Mi et al. (1998). As the impedance sensor's output is proportional to the void fraction, which is related to the flow pattern, its computational cost is relatively low (Rosa et al., 2010). However, it is only applicable to two-phase flow where the conductivities and dielectric coefficients of the gas and liquid are significantly different from each other (Wu et al., 2001). Furthermore, it is sensitive to temperature and requires that the pipe should be composed of nonconducting material. Therefore, it may be difficult to operate in the industrial field.

The purpose of this study is to investigate severe slugging identification in a pipeline-riser system using accelerometer signals. Accelerometers are operated in a nonintrusive fashion and can be transferred to other locations after the initial installation, according to user's desire or operational purpose. In addition, they can result in good classification performance, as the vibration characteristics are considerably different between stable flow and severe slugging, especially during liquid accumulation of the severe slugging process. In this study, a laboratory experiment for severe slugging monitoring in a pipeline-riser system using accelerometers is performed. Although the accelerometers are mounted in the air in the laboratory experiment, they could be applied in both the water and air, such as near the bottom of the riser or close to the topside in a real pipeline-riser system. For early recognition of the flow regime, relatively simple features characterizing flow-

induced vibration (FIV) are presented based on statistical parameters and linear prediction coefficients (LPCs). The classification performance is compared and analyzed according to the signal length for different sensor selections using six accelerometers, one accelerometer at the riser base, and one accelerometer at the top of the riser. Two machine learning algorithms using the SVM and NN are applied to binary classification, and the NN is adopted for multiclass classification to recognize four classes: stable, severe slugging 1 (SS1), and an irregular transition between severe slugging 3 (SS3) and dual-frequency severe slugging (DFSS).

This chapter is organized as follows: Section 4.2 describes the background of severe slugging, including its processes and types. Section 4.3 presents the laboratory experiment in a pipeline-riser system under various environmental conditions of air and water superficial velocities, and presents the characteristics of accelerometer signals. In Section 4.4, a simple description of statistical parameters and LPCs as features for machine learning algorithms is given. In addition, binary and multiclass classification results using the SVM and NN are demonstrated. Section 4.5 summarizes this work and draws conclusions of this chapter.

4.2. Theoretical background

Description of severe slugging

Severe slugging is generally explained by the following four steps: (1) slug formation, (2) slug movement into the separator, (3) blowout, and (4) liquid fallback (Schmidt et al., 1980; Taitel, 1986). Figs. 4-1(a)–(d) present the process of severe slugging and Fig. 4-1(e) shows the pressure at the bottom of the riser (p_B) during one

cycle of severe slugging, where the water and gas superficial velocities are $u_{SW} = 0.19$ m/s and $u_{SG} = 0.59$ m/s, respectively. During slug formation in Fig. 4-1(a), liquid transported from the pipeline starts to accumulate at the bottom of the riser and p_B continuously increases for less than approximately 60 s as shown in Fig. 4-1(e), because the hydrostatic pressure increases by accumulated liquid in the riser. At the same time, the gas is blocked in the pipeline section and compressed. In the second stage of Fig. 4-1(b), the accumulated liquid reaches the top of the riser and moves into the separator while the blocked gas is continuously compressed, and p_B increases to its maximum. When the pressure of the compressed gas surpasses the hydrostatic pressure of the accumulated liquid in the riser, the gas expands and blows out rapidly, as shown in Fig. 4-1(c), and p_B starts to decrease. After the blowout, the remaining liquid in the riser falls back to the riser base as in Fig. 4-1(d) and the slug formation repeats.

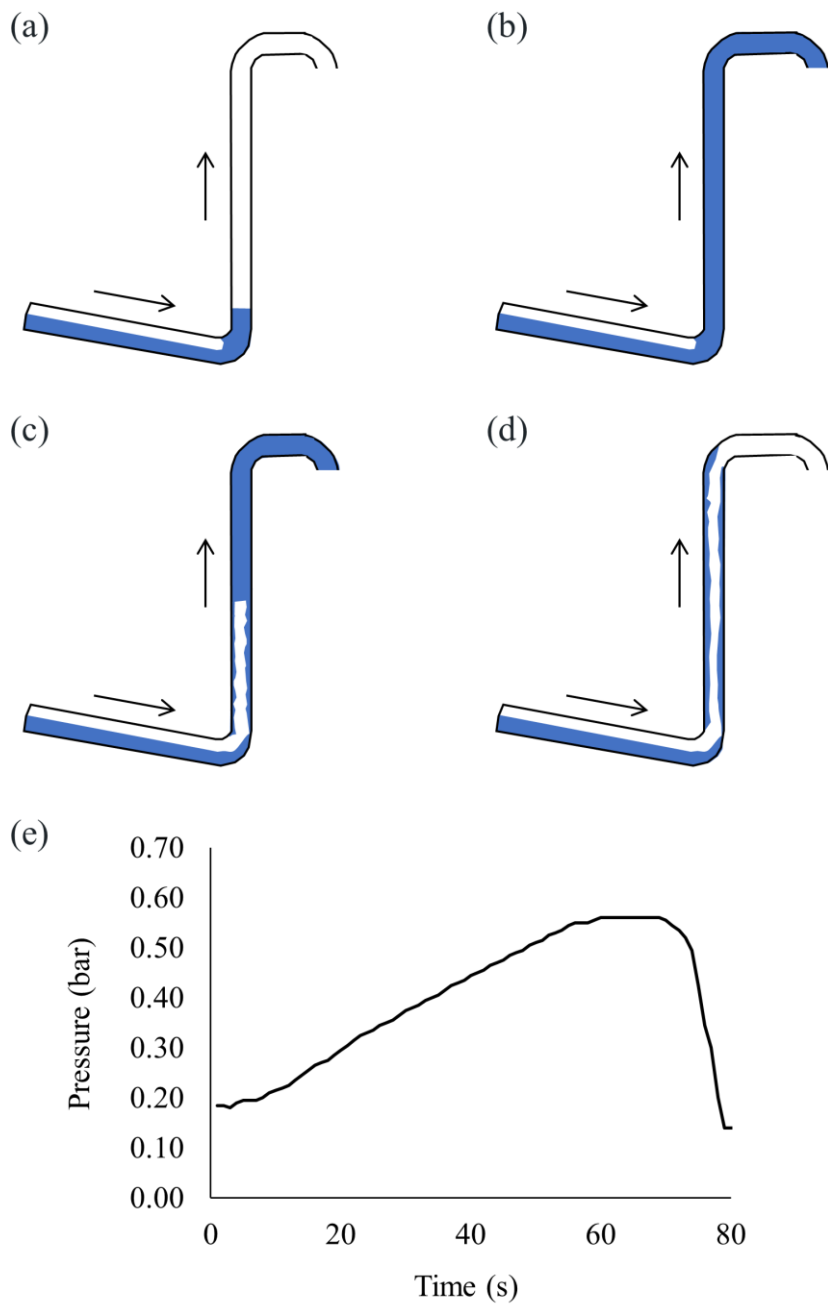


Figure 4-1: Process of severe slugging. (a) Slug formation, (b) slug movement into the separator, (c) blowout, (d) liquid fallback, and (e) pressure at the riser base during one cycle of severe slugging.

In general, severe slugging can be classified into three types (Baliño et al., 2010; Malekzadeh et al., 2012): SS1, severe slugging 2 (SS2), and SS3. SS1 and SS2 are similar, except for the length of the liquid slug. The liquid slug length of SS1 is longer than or equal to the height of the riser, whereas that of SS2 is shorter than the riser length. In case of SS2, the gas penetrates the riser before the liquid reaches the top of the riser, and as a result, the maximum p_B is lesser than that of SS1. SS3, however, is quite different from SS1 and SS2. The gas continuously moves into the riser and creates transient slugs of different sizes. The liquid from the transient slugs falls into the bottom of the riser, accumulates again, and produces a long aerated liquid slug with small bubbles. Similarly, when the compressed gas overcomes the hydrostatic pressure of the stacked aerated liquid slugs, the gas blows out and the cycle repeats. In addition to these three types of severe slugging, Malekzadeh et al. (2012) introduced another type of severe slugging, named DFSS. DFSS is related to SS3 and oscillation (OSC), where OSC is characterized as cyclic pressure fluctuations without intense blowout (Baliño et al., 2010). With respect to DFSS, the liquid content is insufficient to generate SS3 and, at the same time, the gas flow rate is insufficient to maintain OSC. Accordingly, DFSS presents tendencies of both SS3 and OSC, resulting in two different frequencies. The high-frequency component is associated with fluctuations of both SS3 and OSC, because they have their own variations, and the low-frequency element is related to periodic transitions between SS3 and OSC. A typical example of the pressure p_B for DFSS is depicted in Fig. 4-2, as measured in our laboratory experiment at $u_{sw} = 0.15$ m/s and $u_{sg} = 0.99$ m/s. In Fig. 4-2, the period of the high-frequency component is approximately 20 s, and that of the low-frequency element is approximately 100 s. In this study, the unstable flow regimes of SS1, and the irregular transition between DFSS and SS3

are investigated.

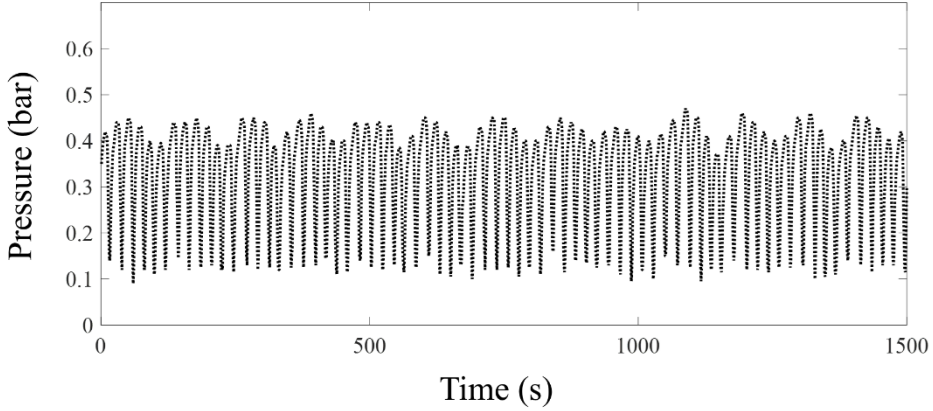


Figure 4-2: Typical pressure signal near the riser base of DFSS. The water and gas superficial velocities are $u_{sw} = 0.15$ m/s and $u_{sg} = 0.99$ m/s, respectively. The period of the high-frequency element is approximately 20 s, and that of low-frequency part is roughly 100 s.

Flow-induced vibration (FIV)

Considering the vertical riser connected to a platform, the transverse deflection $w(y, t)$ is small compared to the length of riser, in which the Euler-Bernoulli theory can be adopted (Paidoussis and Issid, 1974; Onuoha et al., 2018). A small element of the pipe with length δy and the corresponding element of the fluid are presented in Fig. 4-3. When the velocity of the flow is U , the element of the fluid is exposed to internal pressure P , the Coriolis force $2MU \frac{\partial^2 w}{\partial y \partial t}$, the centrifugal force $MU^2 \frac{\partial^2 w}{\partial y^2}$, and shear stress on the internal surface of the pipe $qS\delta y$. And the element of the pipe with bending stiffness EI is exposed to the bending

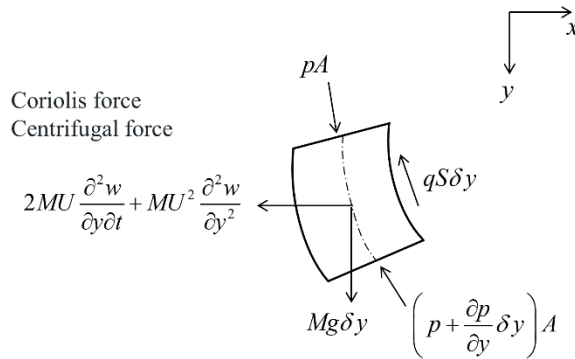
moment M , the transverse shear force in the pipe Q , the shear stress on the internal surface of the pipe $qS\delta y$, and an axial tension of the riser T . From force equilibrium equations for each axis and moment equilibrium equation, the equation of small deflection becomes

$$EI \frac{\partial^4 w}{\partial y^4} - T(y) \frac{\partial^2 w}{\partial y^2} + \rho_f A_i U^2 \frac{\partial^2 w}{\partial y^2} + 2\rho_f U A_i \frac{\partial^2 w}{\partial y \partial t} + A_i P[y(t)] \frac{\partial^2 w}{\partial y^2} + (\rho_r A_r + \rho_f A_i) \frac{\partial^2 w}{\partial t^2} = 0, \quad (4.1)$$

where A_i indicates the internal cross-sectional area of the pipe, A_r is the cross-sectional area of the pipe wall, and densities of the fluid and the riser are ρ_f and ρ_r , respectively. $P[y(t)]$ presents the changing hydrostatic pressure according to the cycle of severe slugging and the tension of the riser $T(y)$ is affected by the submerged weight of the riser and the length of the riser. Although it is difficult to directly relate acceleration $\frac{\partial^2 w}{\partial t^2}$ to other parameters such as pressure or density from Eq. (4.1), several studies of two-phase FIV have drawn that: (1) a major source of internal two-phase FIV is flow turning element (e.g., pipe bending), where it induces sudden changes in momentum flux, pressure fields, and even creates vortices (Miwa et al., 2015); (2) the amplitude of fluctuating force is increased when the flow velocity is increased (Miwa et al., 2015; Liu et al., 2012; Riverin and Pettigrew, 2007); and (3) force signals are increased by momentum flux fluctuations of mixtures, gas and liquid phases (Liu et al., 2012; Riverin and Pettigrew, 2007). When the liquid is accumulated in slug formation and slug production stages, the flow

velocity is decreased and the riser is only composed of liquid phase, which can reduce the FIV in the riser. In blowout stage, the flow velocity is increased and the gas penetrates into the riser. These variations of flow velocity and phases of fluid can induce vibrations in the riser, while the major source of FIV is located at the bottom of the riser corresponding to the flow turning section.

Elements of the fluid



Elements of the pipe

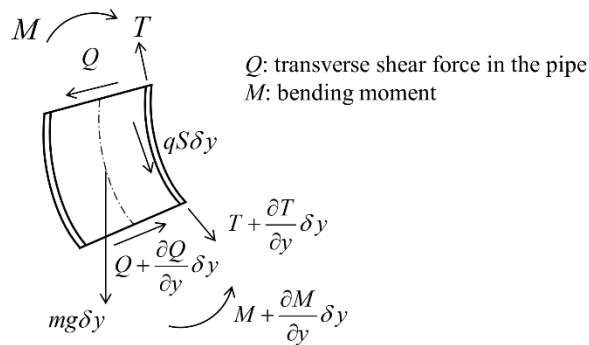


Figure 4-3: Forces and moments on the small element of the pipe and of the corresponding fluid.

4.3. Experimental apparatus and procedure

The experiment was conducted in the flow loop of the Subsea Engineering and Flow Assurance Laboratory at Seoul National University, as shown in Fig. 4-4. The facility consists of a 6.28-m-long downward-inclined pipeline at -15.9° to the horizontal and a 5.6-m-high vertical riser. The pipe is composed of PVC and its inner diameter is 5.08 cm, with 5 mm thickness. The flow loop uses water and air as liquid and gas phases, respectively. The air is compressed to 8 bar by a compressor and stored in pressurized tank. A mass flow controller can control the air injection and an air buffer tank provides enough volume for air. The water is pumped from a water tank using a NETZSCH pump with maximum liquid flow rate 85.14 L/min, which is a constant flow pump producing same flow rate regardless of pressure fluctuation between the front and rear ends. At the top of the riser, a globe type valve is installed to control the flow rate and mitigate the severe slugging. Six accelerometers measuring out-of-plane accelerations were installed at the riser, as indicated by the square markers in Fig. 4-4(a) and the red arrows in Fig. 4-4(b). For convenience, the accelerometers are numbered from 1 to 6 according to the location of the sensors, from the bottom to the top of the riser. Accelerometers 1, 3, 5, and 6 of PCB type 352A60 were installed at $h = 0.27, 1.87, 3.47,$ and 4.22 m from the floor, respectively, and connected to a B&K NEXUS conditioning amplifier 2693. The sensitivity of PCB type 352A60 is 1.02 mV/ms^{-2} and its frequency range is from 5 Hz to 60 kHz. The other two accelerometers, 2 and 4, of B&K type 4384, mounted at $h = 1.07$ and 2.67 m, were connected to a B&K NEXUS conditioning amplifier 2692-C. The sensitivity of B&K type 4384 is 1 pC/ms^{-2} available between 0.1 Hz and 12.6 kHz. The vertical distance between each of the lower five accelerometers was 0.8 m, and

the vertical distance between accelerometers 5 and 6 was 0.75 m. The length of accelerometer data was 10 s and the sampling rate was 50 kHz. In addition, five WIKA model A-10 pressure transmitters were installed as shown in Fig. 4-4(c), and the pressure signal was sampled every second. In this study, only pressure signal obtained from the bottom of the riser is investigated as a reference for the accelerometer data.

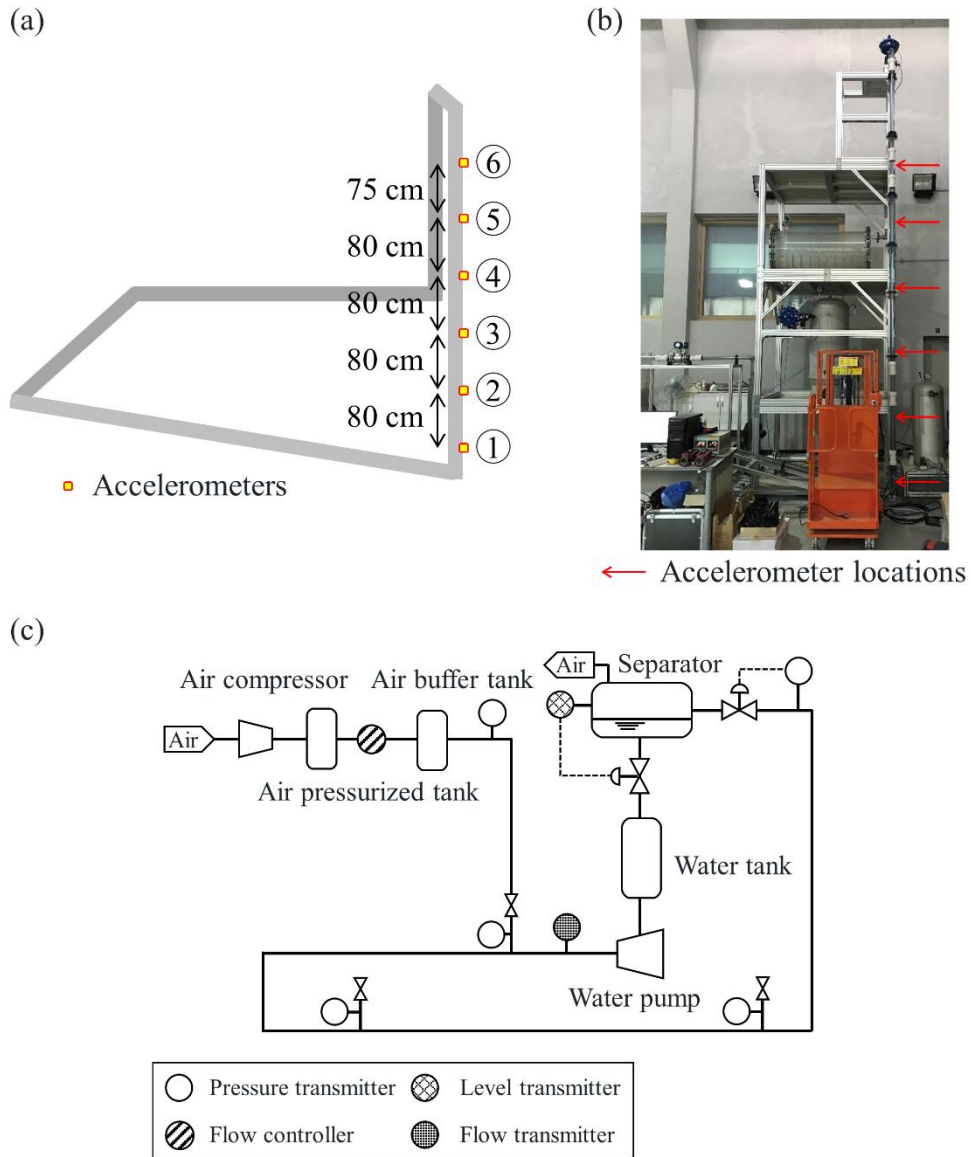


Figure 4-4: Experimental setup. (a) Location of accelerometer sensors, (b) photograph of the vertical riser, and (c) schematic diagram of the flow loop. The six sensor numbers are denoted as 1–6 in (a). The pipe is composed of PVC, and its inner diameter is 5.08 cm with a 5-mm thickness. The length of the inclined pipeline is 6.28 m at -15.9° to the horizontal and the height of the vertical riser is 5.6 m.

To generate the different flow regimes of SS1-1, SS1-2, transition flow, and stable flow, various conditions of water and gas superficial velocities were tested, of which the number of measured data for each environmental condition is summarized in Table 4-1.

Table 4-1: Water and gas superficial velocities and the number of measured data according to the flow regime.

Flow regime	Water superficial velocity (m/s)	Gas superficial velocity (m/s)	Number of measured data
SS1-1	0.09	0.59	1000
		0.7	1000
		0.8	1000
SS1-2	0.19	0.59	1000
		0.7	1000
		0.8	1000
Transition between SS3 and DFSS	0.15	0.7	1000
		0.8	1000
		0.99	1000
Stable	0.26	1.48	250
		1.97	250
Controlled stable	0.09	0.7	500

Fig. 4-5 presents the measured pressure at the riser base (p_B) for each flow condition. Three kinds of the first type of SS1, which is called SS1-1 in this study, occurred under the conditions of $u_{sw} = 0.09$ m/s with $u_{sg} = 0.59, 0.7,$ and 0.8 m/s, as

shown in Figs. 4-5(a)–(c), respectively. When the gas superficial velocity increases, the severe slugging period decreases, because increased gas blocked in the pipeline reduces the time required to exceed the hydrostatic pressure of the accumulated liquid. The second type of SS1, hereinafter referred to as SS1-2, had a longer slug length than that of SS1-1 and three kinds of SS1-2 were generated at $u_{SW} = 0.19$ m/s with $u_{SG} = 0.59, 0.7,$ and 0.8 m/s as shown in Fig. 4-5(d)–(f), respectively. Because the liquid slug length of SS1-2 was longer than that of SS1-1, it needed more gas compression to blowout. Therefore, higher pressure peaks at the riser base are shown in Figs. 4-5(d)–(f), where these peaks indicate gas blowout. For both SS1-1 and SS1-2, the hydrostatic pressures of the fully accumulated liquid at the riser are 0.56 bar. Next, three types of irregular transition between DFSS and SS3 were tested at $u_{SW} = 0.15$ m/s with $u_{SG} = 0.7, 0.8,$ and 0.99 m/s, as shown in Figs. 4-5(g)–(i), respectively. In Fig. 4-5(i), SS3 is developed prior to approximately 200 s and DFSS is presented later than 200 s, where the high frequency of DFSS is approximately 20 s and the low frequency of DFSS is approximately 100 s. Additionally, two conditions of the stable regime were investigated at $u_{SW} = 0.26$ m/s with $u_{SG} = 1.48$ and 1.97 m/s, as shown in Figs. 4-5(j) and (k). p_B ranges from 0.2 to 0.3 bar, which is completely different from that of severe slugging, which fluctuates between 0.2 and 0.6 bar. Lastly, a controlled stable condition was implemented. After SS1-1 was generated at $u_{SW} = 0.09$ m/s with $u_{SG} = 0.7$ m/s, a choke valve installed at the top of the riser was operated to eliminate the severe slugging. Choking the valve transforms unstable flow into stable flow by increasing the pressure difference across the choke (Farghaly, 1987; Pedersen et al., 2017) with a proportional-integral-derivative controller. The data measured after flow stabilization were applied to a

classification analysis of the stable flow regime. For each severe slugging condition, 1,000 data samples were collected, considering that the occurrence interval of severe slugging was approximately 100 s. As a result, approximately 100 cycles of severe slugging were obtained. Meanwhile, 250 samples were acquired for conventional stable flow and 500 samples were measured for controlled stable flow, considering the stabilizing time. Because there was no cyclic process for stable flow, the number of measured data was smaller than that of severe slugging.

Figs. 4-6(a) and (b) provide comparisons of p_B and a signal from accelerometer 1 near the riser base during severe slugging cycles of SS1-1 at $u_{sw} = 0.09$ m/s with $u_{sg} = 0.59$ m/s and SS1-2 at $u_{sw} = 0.19$ m/s with $u_{sg} = 0.59$ m/s, respectively. The black dotted line indicates p_B and the blue solid line shows the vibration signal of accelerometer 1. Although the signals of vibration and pressure are not perfectly synchronized owing to the different data acquisition systems, they present comparable trends of severe slugging. When the liquid starts to accumulate at the riser, which is a starting point of pressure increase, the vibration drastically decreases because an FIV diminishes rapidly. After the blowout, the FIV is developed as the gas penetrates the riser and the pressure starts to decrease. In accordance with the cyclic severe slugging process, the vibration signals also reveal cyclical trend.

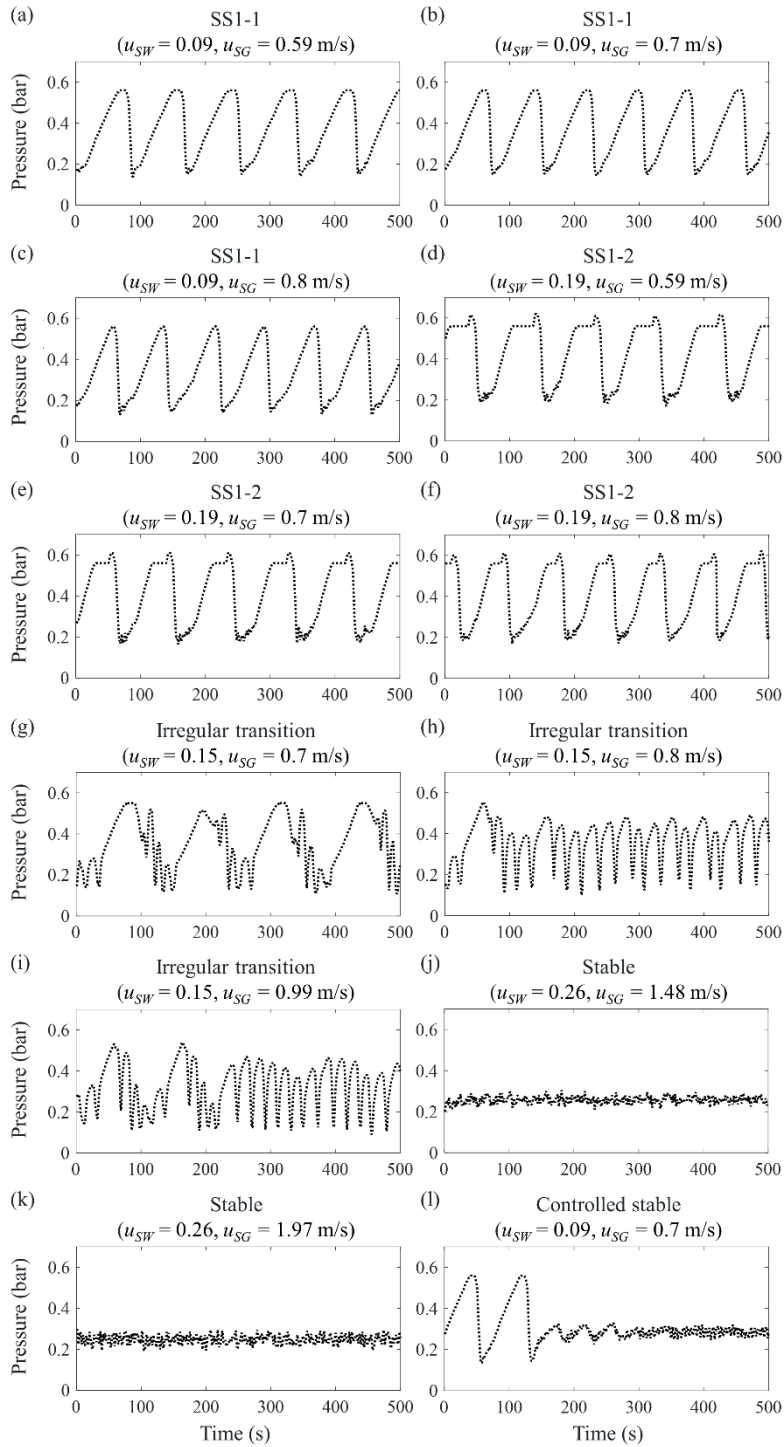


Figure 4-5: . Measured pressure at the riser base for each flow regime: (a)–(c) SS1-

1 at $u_{SW} = 0.09$ m/s with $u_{SG} = 0.59, 0.7,$ and 0.8 m/s; (d)–(f) SS1-2 at $u_{SW} = 0.19$ m/s with $u_{SG} = 0.59, 0.7,$ and 0.8 m/s; (g)–(i) irregular transition between SS3 and DFSS at $u_{SW} = 0.15$ m/s with $u_{SG} = 0.7, 0.8,$ and 0.99 m/s; (j)–(k) stable flow at $u_{SW} = 0.26$ m/s with $u_{SG} = 1.48$ and 1.97 m/s; and (l) controlled stable flow after SS1-1 generation at $u_{SW} = 0.09$ m/s with $u_{SG} = 0.7$ m/s.

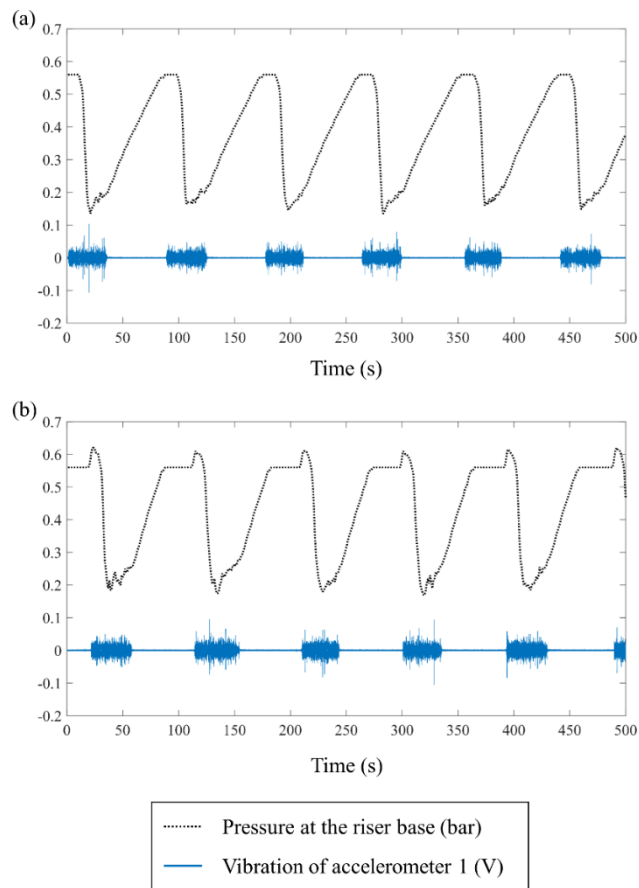


Figure 4-6: Comparison of the pressure at the riser base and the signals from accelerometer 1 for (a) SS1-1 at $u_{SW} = 0.09$ m/s with $u_{SG} = 0.59$ m/s and (b) SS1-2 at $u_{SW} = 0.19$ m/s with $u_{SG} = 0.59$ m/s. The black dotted line indicates the

pressure and the blue solid line indicates the vibration.

Fig. 4-7 illustrates vibration signals of SS1-1 at $u_{sw} = 0.09$ m/s with $u_{sg} = 0.59$ m/s near the blowout process, when the FIV begins to be generated. The signals acquired from accelerometers 1–6 are depicted in Figs. 4-7(a)–(f), respectively. The FIV after the blowout is acquired from approximately 1.2 s for accelerometer 1 and 5.6 s for accelerometer 6. The internal two-phase FIV is mainly due to the presence of a flow-turning section. It changes the momentum flux and pressure fields in a short time, thereby generating large forces (Cargnelutti et al., 2010; Miwa et al., 2015). Consequently, in the pipeline-riser system of this experiment, the main source of vibration was located at the bottom of the riser, at the turning zone connecting the inclined pipeline and the vertical riser. As shown in Fig. 4-7, the signal amplitude of accelerometer 1 close to the bottom is larger than those of the other sensors. In addition, to investigate the characteristics of the flow noise source, power spectra from the signals of accelerometer 1 about SS1-1 at $u_{sw} = 0.09$ m/s with $u_{sg} = 0.59$ m/s are investigated. Fig. 4-8 shows two typical spectra of the no-vibration part during liquid accumulation (black solid line) and the vibration part after the blowout (red dotted line), which are produced using signals of length 10 s. The x-axis represents the frequency on a logarithmic scale and the y-axis shows the power spectrum in decibels. As shown in Fig. 4-8, the energy of the FIV dominates below 10 kHz, especially near 1.5 kHz and 20 Hz.

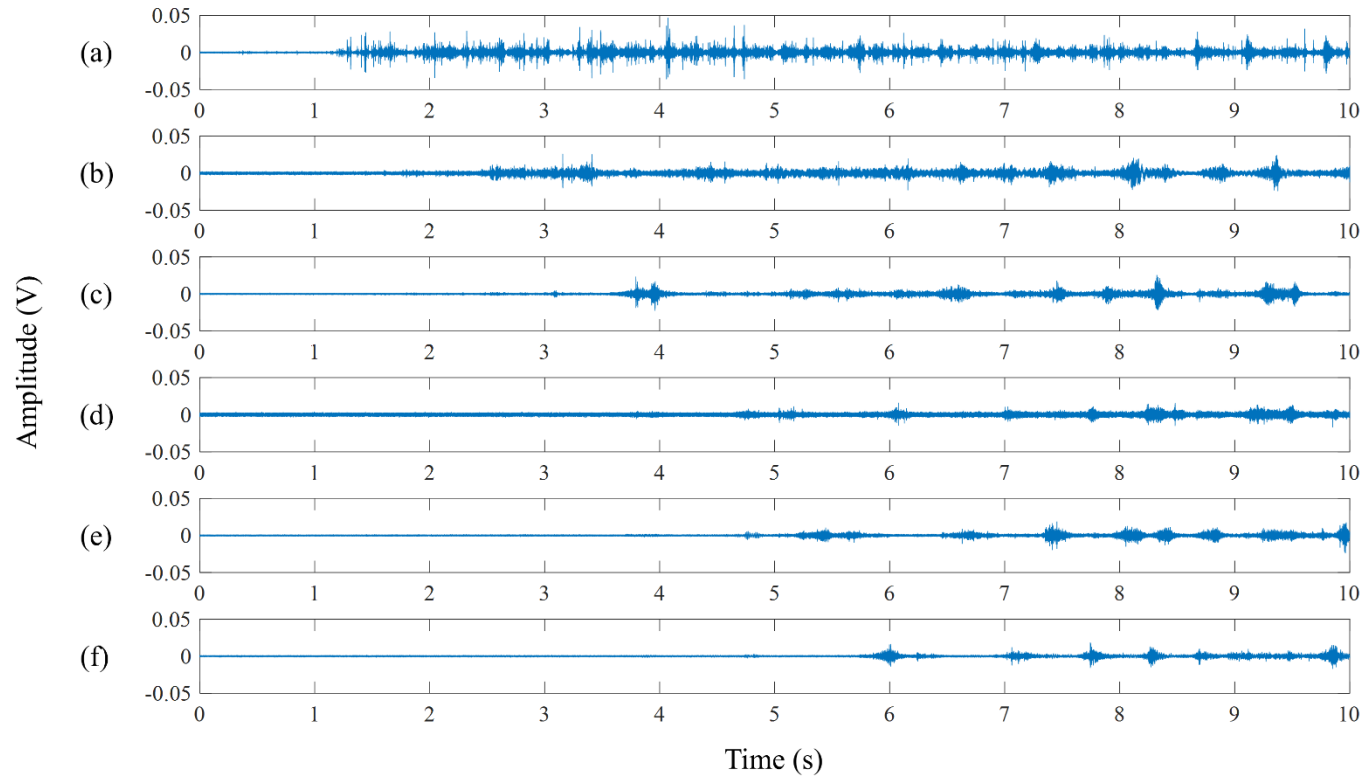


Figure 4-7: Vibration signals from accelerometers 1–6 in (a)–(f), respectively. The flow is generated at $u_{SW} = 0.09$ m/s with $u_{SG} = 0.59$ m/s.

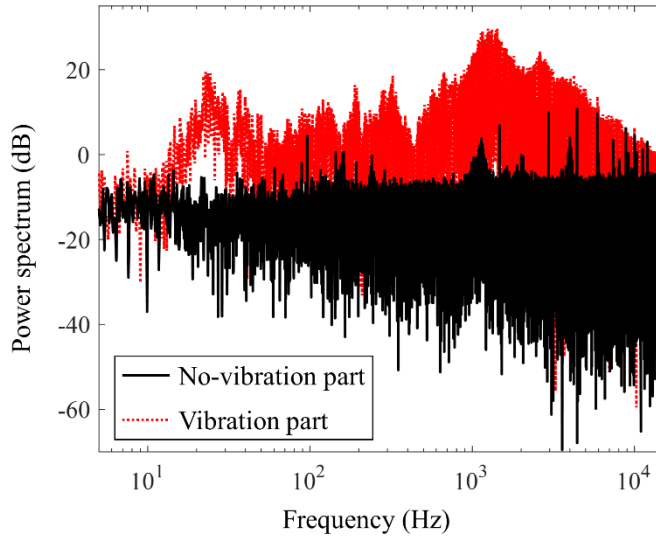


Figure 4-8: Typical spectrum of FIV. The red dotted line presents the spectrum of FIV and the black solid line is the noise spectrum of the no-vibration part. Most energy of FIV is distributed below 10 kHz, especially near 1.5 kHz and 20 Hz.

4.4. Classification method

Statistics and linear prediction coefficients of feature vectors

The vibration signals acquired from the accelerometers provide information about the flow regime, and in particular, the data obtained during the liquid accumulation of the severe slugging process play an important role in the flow recognition. For fast recognition of severe slugging, five simple statistical parameters (Jung et al., 2018) and linear prediction coefficients (LPCs) are investigated instead of using many types of feature extraction methods such as power spectral density (Ye and Guo, 2013) or wavelet denoising (Wu et al., 2001). The mean, variance, skewness, kurtosis, root mean square (RMS), and fifth order of LPCs

are calculated from the absolute values of measured vibrations $x(t) = |s(t)|$, where $s(t)$ is the raw vibration signal. The mean and variance of $x(t)$ are defined as $F_1 = E[t] = \frac{1}{T} \int_0^T x(t) dt$ and $F_2 = E[(t - F_1)^2]$, respectively (Bendat and Piersol, 2011). Similarly, the skewness and kurtosis are calculated as

$$F_n = E \left[\left(\frac{(t - F_1)}{\sqrt{F_2}} \right)^n \right], \quad (4.2)$$

where $n = 3$ and 4 represent the skewness and kurtosis, respectively (Gubner, 2006). The RMS is defined as (Zill et al., 2006)

$$F_5 = \sqrt{\frac{1}{T} \int_0^T \{x(t)\}^2 dt}. \quad (4.3)$$

Meanwhile, linear prediction is a technique to estimate a future value by using previous values. The predicted value is computed by a linear combination of weighted past values $x(n-1)$, $x(n-2)$, ..., $x(n-p)$. The linearly predicted value $\hat{x}(n)$ is defined as (Proakis and Manolakis, 1996)

$$\hat{x}(n) = -\sum_{k=1}^p a_p(k) x(n-k), \quad (4.4)$$

where $-a_p(k)$ are weights referred to as LPCs of order p . In this study, the order

p is fixed as 5 because it leads to better classification performance. For $1 \leq k \leq 5$, $-a_5(k)$ are defined as features F_i ($6 \leq i \leq 10$). Ten parameters of feature vectors are listed in Table 4-2. Meanwhile, to consider features of frequency domain, classification analysis based on thirteen parameters with additional features, mean, RMS, and maximum of frequency domain signals is presented in appendix A.3.

Table 4-2: Summary of feature parameters. $x(t)$ is defined as $x(t) = |s(t)|$ and $-a_i(i - 5)$ are the LPCs of Eq. (4.4).

Feature		Equation
F_1	Mean	$F_1 = E[t] = \frac{1}{T} \int_0^T x(t) dt$
F_2	Variance	$E[(t - F_1)^2]$
F_3	Skewness	$E[((t - F_1)/\sqrt{F_2})^3]$
F_4	Kurtosis	$E[((t - F_1)/\sqrt{F_2})^4]$
F_5	RMS	$\sqrt{\int_0^T \{x(t)\}^2 dt / T}$
F_i ($6 \leq i \leq 10$)	LPC	$-a_5(i-5)$

Feature vector extraction

To classify the flow regime using a short time interval, features were extracted from signals clipped to 7, 5, and 2.5 s in length from the raw data of 10 s length. For the clipped signals of 7 s length, the raw data were divided into two parts of the time intervals $[0, 7]$ and $[3, 10]$, and the data were split into the intervals $[0, 5]$ and $[5, 10]$

for the 5-s-long clipped signals. In the case of the 2.5-s-long clipped signals, the data were clipped as the intervals [0, 2.5] and [2.5, 5], where the last 5 s were not used. The performance of using signals divided into the intervals [0, 2.5], [2.5, 5], [5, 7.5], and [7.5, 10] is quite similar to that of the analysis without using the last 5 s (not shown in this dissertation). We apply the clipped signals of the intervals [0, 2.5] and [2.5, 5] to balance the size of the feature and the cyclic pattern of severe slugging with the signals of 7 and 5 s.

Ten parameters of a feature vector, including mean, variance, skewness, kurtosis, RMS, and fifth-order LPCs, for each clipped signal were calculated per accelerometer. If the number of accelerometers is A and the number of clipped signals is N , an input of the learning algorithms becomes an $N \times K$ matrix, where K is the dimension of the feature computed by multiplying A and the total number of feature parameters 10 in Table 4-2. For example, if we use six accelerometers with 100 clipped signals, the input feature is a 100×60 matrix.

Fig. 4-9 illustrates a distribution example of the mean and variance of 250 clipped signals of 7 s in the time interval [0, 7] obtained from accelerometer 1, comparing stable flow at $u_{sw} = 0.26$ m/s with $u_{sg} = 1.48$ m/s and SS1-1 at $u_{sw} = 0.09$ m/s with $u_{sg} = 0.59$ m/s. The x-axis represents the mean and the y-axis shows the variance, where the maximum value is 1 for the mean parameter because data are normalized. The red circle markers indicate SS1-1 and the blue triangle markers represent stable flow. As shown in Fig. 4-9, the distributions of the two categories are quite separable, in which the values of the mean and variance of stable flow are higher than those of severe slugging because stable flow constantly generates vibration. With respect to the vibration signals of severe slugging, there are two distinct regions: the no-vibration parts of liquid accumulation and vibration parts

after the blowout. Consequently, the mean and variance of severe slugging are distributed from the lower values at the no-vibration parts to the higher values at the vibration parts near the distribution of stable flow. A significant role of the classifier is to separate the flow regimes carefully in the vicinity of the vibration parts, where the signals for stable flow and severe slugging demonstrate similar patterns.

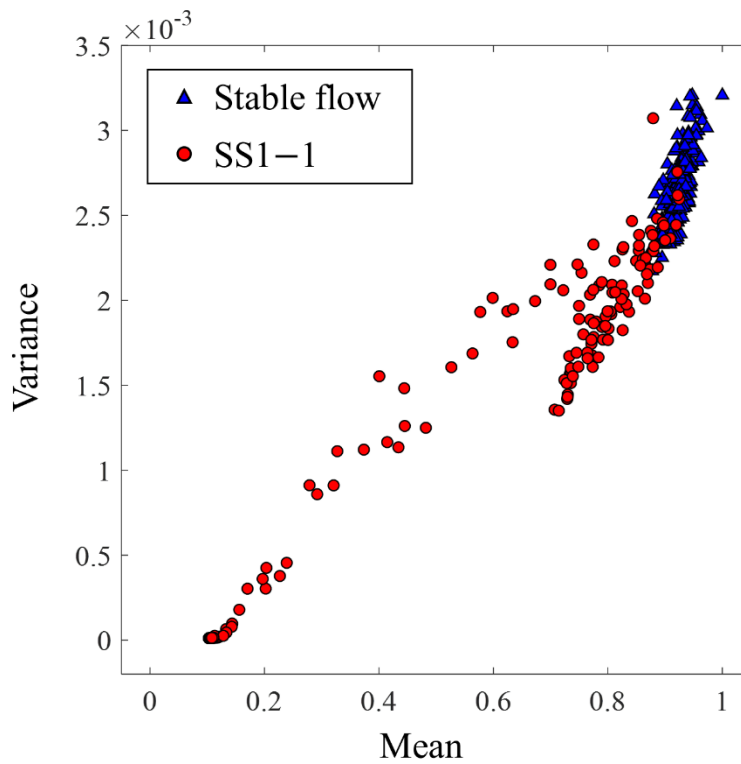


Figure 4-9: Distribution of mean and variance features for stable flow ($u_{sw} = 0.26$ m/s, $u_{sg} = 1.48$ m/s) and SS1-1 ($u_{sw} = 0.09$ m/s, $u_{sg} = 0.59$ m/s). The red circle markers represent SS1-1 and the blue triangle markers represent stable flow.

Binary and multiclass classification method

The supervised learning algorithms of the SVM was adopted to classify the

stable flow and severe slugging. The SVM was trained and implemented using the MATLAB statistics and machine learning toolbox. The SVM is a binary classification algorithm that maximizes a margin given by the smallest distance between the decision hyperplane and any of the data (Bishop, 2006). The SVM finds sparse solutions called support vectors that predict new data with a subset of training data. It solves the optimization problem expressed as (Burges, 1998)

$$\left\{ \begin{array}{l} \max \left(\sum_{i=1}^N \alpha_i - \frac{1}{2} \sum_{i=1}^N \sum_{j=1}^N \alpha_i \alpha_j t_i t_j K(\mathbf{x}_i, \mathbf{x}_j) \right) \\ \text{s.t. } \sum_{i=1}^N \alpha_i t_i = 0, \quad 0 \leq \alpha_i \leq C, \quad i = 1, \dots, N \end{array} \right., \quad (4.5)$$

where \mathbf{x}_i are input vectors; t_i are class labels presented as 1 or -1 ; α_i are Lagrange multipliers related to the support vectors; C is a parameter determined by the user's desire, where a larger value of C gives a higher penalty to errors; and K is a kernel function. Then, the decision hyperplane is expressed as

$$f(\mathbf{x}) = \sum_{i=1}^{N_s} \alpha_i t_i K(\mathbf{x}_s, \mathbf{x}_i) + b. \quad (4.6)$$

In Eq. (4.6), \mathbf{x}_s are support vectors, N_s is the number of support vectors, and b is the bias. From the sign of $f(\mathbf{x})$, the flow regime can be determined.

The other machine learning algorithm, NN, was applied to multiclass classifications using the MATLAB neural network tool box. The NN contains hidden units $\mathbf{h} = g(\mathbf{W}^T \mathbf{x} + \mathbf{c})$, where \mathbf{W} represent weights, \mathbf{c} are biases, and g is an

activation function. A commonly used sigmoid function is applied as activation function. The size of the input layer is K ($A \times 10$) and the output layer has two neurons for stable flow and severe slugging. Meanwhile, hyper-parameters for the SVM and NN such as the kernel function, parameters of the kernel function, layers, and nodes were optimized to minimize the five-fold cross-validation errors.

Two hundred and twenty-five samples were chosen from each of the two stable conditions at $u_{sw} = 0.26$ m/s with $u_{sg} = 1.48$ and 1.97 m/s. After the clipping process, the number of data is doubled because an original sample was clipped into two parts such as $[0, 5]$ and $[5, 10]$ for 5-s-long signals. Accordingly, 900 data were generated for the stable flow class, which are computed as 225 (samples from each stable condition) $\times 2$ (flow conditions) $\times 2$ (clipping process). Similarly, the severe slugging class was constructed from nine conditions of the severe slugging as listed in Table 4-1. In machine learning algorithms, it is important to balance the number of data for each class. Therefore, 50 samples from each of the nine severe slugging conditions were selected sequentially to produce a total of 900 data, calculated as 50 (samples from each severe slugging condition) $\times 9$ (flow conditions) $\times 2$ (clipping process).

4.5. Classification results and discussion

Binary classification results

In this study, three cases of adopting accelerometers are investigated using: (1) all six accelerometers; (2) accelerometer 1 at the riser base; and (3) accelerometer 6 at the top of the riser. Therefore, the dimension of the feature K is 60 or 10, according

to the number of accelerometers. The purpose of the analysis applying accelerometer 1 and 6 is to examine the effect of sensor location and the possibility of adopting a small number of sensors.

Table 4-3 presents the binary classification results of the SVM. The input is a 900×60 matrix for six accelerometers and a 900×10 matrix for one accelerometer. The averaged accuracy, the accuracy for stable flow, and that for severe slugging are demonstrated according to the signal length based on the accelerometer selection. Because long time signals have more information about the flow regime, they result in better performance than those of short time signals. Hence, using 7-s-long signals with six accelerometers yields the best performance, where the averaged accuracies are approximately 99.78% for the SVM. When the signal length decreases to 2.5 s, the averaged accuracies also degenerate to 96.89% for the SVM. Furthermore, the accuracies for stable flow are higher than those for severe slugging. This is because a main factor distinguishing between the two classes is the no-vibration parts during the liquid accumulation of severe slugging, whereas identifying the vibration parts between severe slugging and stable flow is more complicated. Therefore, the misclassification probability of severe slugging increases in the vicinity of the vibration parts, as shown in Fig. 4-9. Moreover, the sensor location can affect the performance because the major source of FIV is located at the bottom of the riser. In Table 4-3, the signals from accelerometer 1, close to the riser base, lead to better performance than the signals from accelerometer 6, near the top of the riser, because of the clearer distinctions between the vibration parts and no-vibration parts. The optimized parameters of SVM are presented in appendix A.2.

Table 4-3: Binary classification results of the SVM.

Accelerometer	Length of signals (s)	Averaged accuracy (%)	Accuracy for stable flow (%)	Accuracy for severe slugging (%)
1-6	7	99.78	99.89	99.67
	5	98.83	99.22	98.44
	2.5	96.89	98.22	95.56
1	7	95.39	98.56	92.22
	5	94.22	96.44	92
	2.5	90.67	95.7	85.56
6	7	88	96.89	79.11
	5	85.78	96.56	75
	2.5	82.22	92.67	71.78

In the aforementioned results, only 50 samples were extracted out of 1,000 data for each severe slugging condition to balance the size of the features with the stable flow class. To investigate the performance difference according to sample group selection in the severe slugging data, additional analysis is performed on clipped signals of length 7 s obtained by using all six accelerometers through the SVM. The results are presented in Table 4-4, where the first column indicates the group number of the samples of severe slugging. For each sample group, a different sequence of 50 samples was extracted from each severe slugging condition, and the data of the stable class were the same as in Table 4-3. For example, the first 50 samples were selected as group 1, the next 50 samples were chosen as group 2, and the next 50 samples were used as the subsequent group. This was repeated 10 times to check a total of 500 samples. The averaged accuracies of different groups are similar, which have a maximum of 99.78% and a minimum of 98.67%. This is because each group of samples are in time series composed of approximately 4–6 cycles of severe slugging.

Therefore, the sample group selection cannot significantly affect the classification performance by similar cyclic patterns.

Table 4-4: Binary classification results of the SVM for signals of length 7 s with six accelerometers.

Data group	Averaged accuracy (%)
1	98.67
2	98.94
3	99.06
4	98.83
5	99.44
6	99.39
7	99.5
8	99.33
9	99.56
10	99.78
Maximum	99.78
Minimum	98.67
Average	99.25

Finally, the effect of the controlled stable condition was tested by converting the features of stable flow to include three stable flow conditions, as listed in Table 4-1. One hundred and fifty samples from each stable flow conditions were selected and clipped according to signal length. The number of data for the stable class is 900, calculated as 150 (samples from each stable condition) \times 3 (flow conditions) \times 2 (clipping process), and the features of severe slugging are same as in Table 4-3.

Table 4-5 presents the classification results of the SVM. The averaged accuracies are comparable to those of the previous analyses in Table 4-3. The FIV of the controlled stable condition presents less continuous patterns than the conventional stable flow, which is associated with the valve opening. In most cases, it leads to higher accuracies of severe slugging and lower accuracies of stable flow than those of the previous analyses in Table 4-3. Similarly, the accuracies degenerate as the signal length decreases.

Table 4-5: Binary classification results of the SVM including controlled stable regime.

Accelerometer	Length of signals (s)	Averaged accuracy (%)	Accuracy for stable flow (%)	Accuracy for severe slugging (%)
1-6	7	99.78	99.67	99.89
	5	98.94	99.11	98.78
	2.5	97.39	98.44	96.33
1	7	95.72	97.22	94.22
	5	94.5	96.22	92.78
	2.5	90.39	92.33	88.44
6	7	88.44	95.22	81.67
	5	86.89	96	77.78
	2.5	84.17	92.22	76.11

In the recent study of Zou et al. (2017), the shortest signals of 6.8 s were tested based on the trained LS-SVM using 8.99-s-long signals. The averaged accuracy was 93.78%, where the accuracy of unstable flow was 94.9% and that of stable flow was 90.57%. Apart from the machine learning algorithm, there are some differences from this study: (1) the data were acquired from three types of differential pressures of the

riser; (2) the number of each class for binary classification was different; (3) the unstable flow regime composition was different, which had SS1, SS2, SS3, OSC, and unstable cycles of an irregular region. Although direct comparison is difficult because of the aforementioned differences, it is worth mentioning that our results obtained with short signals show comparable performance to their results. Overall, this presents satisfactory performance is achieved using accelerometers in binary classification; in particular, the performance obtained by using 2.5-s-long signals shows the possibility of real-time monitoring.

Multiclass classification results

The main objective of multiclass classification using the NN is to recognize stable flow, SS1-1, SS1-2, and the irregular transition between SS3 and DFSS. The features of the stable class cover two stable flow conditions at $u_{sw} = 0.26$ m/s with $u_{sg} = 1.48$ and 1.97 m/s. Two hundred and forty samples were extracted from each stable flow condition and doubled by a clipping process. Accordingly, 960 data in total were computed as 240 (samples from each stable condition) $\times 2$ (flow conditions) $\times 2$ (clipping process). In the case of SS1-1, 160 samples were extracted from three conditions of $u_{sw} = 0.09$ m/s with $u_{sg} = 0.59, 0.7,$ and 0.8 m/s. A total of 960 data were produced by 160 (samples from each severe slugging condition) $\times 3$ (flow conditions) $\times 2$ (clipping process), and the processes of data generation of SS1-2 and irregular transition are same as that of SS1-1. Table 4-6 presents the multiclass classification results with six accelerometers using the NN. The averaged accuracies range from 94.11% to 97.16% according to the signal length. The accuracies for stable flow are higher than those of severe slugging, which results

from the vibration parts after the blowout of each severe slugging being comparable to each other. This also renders the averaged accuracies of multiclass classification slightly lower than those of binary classification. The optimized parameters are presented in appendix A.2.

Table 4-6: Multiclass classification results of the NN with six accelerometers.

Accuracy (%)	Length of samples (s)		
	7	5	2.5
Averaged accuracy (%)	97.16	96.85	94.11
Accuracy for stable flow (%)	99.48	99.17	98.65
Accuracy for SS1-1 (%)	95.63	95.73	91.35
Accuracy for SS1-2 (%)	97.29	96.67	94.27
Accuracy for irregular transition (%)	96.25	95.83	92.19

4.6. Summary and conclusions

In this chapter, the severe slugging recognition in a pipeline-riser system using signals from accelerometers was proposed. Vibrations were obtained from the bottom to the top of the vertical riser under various environmental conditions generated by different water and gas superficial velocities. For online recognition of the flow regime, the simple features of mean, variance, skewness, kurtosis, RMS, and fifth-order LPCs were extracted from the absolute values of the vibration signals. The SVM was used for binary classification and the NN was adopted in multiclass

classification to recognize stable flow, SS1-1, SS1-2, and an irregular transition between SS3 and DFSS. The hyper-parameters were optimized to minimize the five-fold cross-validation errors.

Our classifiers show the best performance in signals of length 7 s with six accelerometers. Although the performance degenerates for short time signals, the averaged accuracy of binary classification of 2.5-s-long signals with six accelerometers is quite high, at 97%, using the SVM. The recognition rate of stable flow tends to be higher than that of severe slugging, because separating the vibration parts of severe slugging and stable flow is more intricate. When the number of accelerometers decreases to one, the accuracy of accelerometer 1 near the riser base is higher than that of accelerometer 6 close to the top of the riser. This is because the major source of FIV is located at the bottom of the riser, the flow-turning section of the structure. As a result, signals from the accelerometer near the riser base have a clearer distinction between the vibration and no-vibration parts, thereby yielding better classification performance. The averaged accuracies for multiclass classification using six accelerometers range from 94.11% to 97.16% according to the signal length. As identifying each severe slugging is more complicated owing to their similar tendencies of the vibration parts after the blowout, the recognition rates of multiclass classification are slightly lower than those of binary classification.

The success of early recognition of severe slugging is based on the measuring device and simple features. Our results show that the use of signals from accelerometers leads to good performance, as vibration measurements are a great discriminator in the no-vibration parts during the liquid accumulation state of the severe slugging cycle. Based on our analysis, adding information from accelerometer signals can further improve the reliability of established severe slugging monitoring

systems.

Meanwhile, the effect of additional features using frequency domain signals is presented in appendix A.3. Although we expected that the modified feature sets could improve classification performance, there has no clear differences from the results of original features, because original features are sufficient to recognize the severe slugging in this study. Further studies of feature selection can be developed, which could be useful to identify various flow regimes, not only for stable flow and severe slugging, but also for oscillation, annular flow, or churn flow. In addition, further research can be extended to improve performance using sensors at the upper section of the riser for development of monitoring system above the sea level.

4.7. Acknowledgments

This chapter, in full, is a submitted paper in Ocean Engineering, 2019, with authors S. Jung, H. Yang, K. Park, Y. Seo, and W. Seong, “Monitoring severe slugging in pipeline-riser system using accelerometers for application in early recognition”

Bibliography

- Baliño, J.L., Burr, K.P., Nemoto, R.H., 2010. Modeling and simulation of severe slugging in air-water pipeline-riser systems. *Int. J. Multiph. Flow* 36, 643–660.
- Bendat, J.S., Piersol, A.G., 2011. *Random Data: Analysis and Measurement Procedures*, John Wiley & Sons.
- Bishop, C., 2006. *Pattern Recognition and Machine Learning*. Springer-Verlag New York.
- Blaney, S., Yeung, H., 2008. Investigation of the exploitation of a fast-sampling single gamma densitometer and pattern recognition to resolve the superficial phase velocities and liquid phase water cut of vertically upward multiphase flows. *Flow Meas. Instrum.* 19, 57–66.
- Burges, C.J., 1998. A tutorial on support vector machines for pattern recognition. *Data Min. Knowl. Discov.* 2, 121–167.
- Cargnelutti, M.F., Belfroid, S.P.C., Schiferli, W., 2010. Two-phase flow-induced forces on bends in small scale tubes. *J. Press. Vessel Technol.* 132, 041305.
- Farghaly M.A., 1987. Study of severe slugging in real offshore pipeline riser pipe

- system. In: 5-th Society of Petroleum Engineers Middle East Oil Show.
- Goudinakis, G., 2004. Investigation on the use of raw time series and artificial neural networks for flow pattern identification in pipelines. Cranfield University, Ph.D. thesis.
- Gubner, J.A., 2006. Probability and Random Processes for Electrical and Computer Engineers, Cambridge University Press.
- Hernández, L., Juliá, J.E., Chiva, S., Paranjape, S., Ishii, M., 2006. Fast classification of two-phase flow regimes based on conductivity signals and artificial neural networks. *Meas. Sci. Technol.* 17, 1511–1521.
- Hill, T.J., Wood, D.G., 1994. Slug flow: occurrence, consequences, and prediction. In: University of Tulsa Centennial Petroleum Engineering Symposium.
- Juliá, J.E., Liu, Y., Paranjape, S., Ishii, M., 2008. Upward vertical two-phase flow local flow regime identification using neural network techniques. *Nucl. Eng. Des.* 238, 156–169.
- Jung, S., Seong, W., Lee, K., 2018. Damage detection on an aluminum plate from the cross-correlation of diffuse field using the support vector machine. *Ocean Eng.* 161, 88–97.
- Kang, C., Wilkens, R., Jepson, W.P., 1996. The effect of slug frequency on

corrosion in high pressure, inclined pipelines. In: CORROSION 96. NACE International.

Malekzadeh, R., Henkes, R.A.W.M., Mudde, R.F., 2012. Severe slugging in a long pipeline-riser system: experiments and predictions. *Int. J. Multiph. Flow* 46, 9–21.

Mi, Y., Ishii, M., Tsoukalas, L.H., 1998. Vertical two-phase flow identification using advanced instrumentation and neural networks. *Nucl. Eng. Des.* 184, 409–420.

Miwa, S., Mori, M., Hibiki, T., 2015. Two-phase flow induced vibration in piping systems. *Prog. Nucl. Energy* 78, 270–284.

Onuoha, M., Li, Q., Duan, M., 2018. On the interaction between severe slug buildup and dynamic response of a submerged top-tensioned riser. *Ocean Eng.* 164, 683-697.

Paidoussis, M. P., Issid, N. T., 1974. Dynamic stability of pipes conveying fluid. *J. Sound. Vib.* 33(3), 267-294.

Pedersen, S., Durdevic, P., Yang, Z., 2017. Challenges in slug modeling and control for offshore oil and gas productions: a review study. *Int. J. Multiph. Flow* 88, 270–284.

- Proakis, J.G., Manolakis, D.G., 1996. Digital Signal Processing: Principles, Algorithms and Applications, New York: Macmillan.
- Rosa, E.S., Salgado, R.M., Ohishi, T., Mastelari, N., 2010. Performance comparison of artificial neural networks and expert systems applied to flow pattern identification in vertical ascendant gas-liquid flows. *Int. J. Multiph. Flow* 36, 738–754.
- Schmidt, Z., Brill, J.P., Beggs, H.D., 1980. Experimental study of severe slugging in a two-phase-flow in a pipeline-riser pipe system. *Soc. Pet. Eng. J.* 20, 407–414.
- Schmidt, Z., Doty, D.R., Dutta-Roy, K., 1985. Severe slugging in offshore pipeline riser-pipe systems. *Soc. Pet. Eng. J.* 25, 27–38.
- Sun, J.Y., Jepson, W.P., 1992. Slug flow characteristics and their effect on corrosion rates in horizontal oil and gas pipelines. In: Annual Technical Conference and Exhibition of the Society of Petroleum Engineers.
- Taitel, Y., 1986. Stability of severe slugging. *Int. J. Multiph. Flow* 12, 203–217.
- Trafalis, T.B., Oladunni, O., Papavassiliou, D. V., 2005. Two-phase flow regime identification with a multiclassification support vector machine (SVM) model. *Ind. Eng. Chem. Res.* 44, 4414–4426.

- Wu, H., Zhou, F., Wu, Y., 2001. Intelligent identification system of flow regime of oil-gas-water multiphase flow. *Int. J. Multiph. Flow* 27, 459–475.
- Ye, J., Guo, L., 2013. Multiphase flow pattern recognition in pipeline-riser system by statistical feature clustering of pressure fluctuations. *Chem. Eng. Sci.* 102, 486–501.
- Yocum, B.T., 1973. Offshore riser slug flow avoidance: mathematical and optimization. In: *Second Annual European Meeting of the Society of Petroleum Engineers*.
- Zill, D.G., Wright, W.S., Cullen, M.R., 2006. *Advanced Engineering Mathematics*, Jones & Bartlett Learning.
- Zou, S., Guo, L., Xie, C., 2017. Fast recognition of global flow regime in pipeline-riser system by spatial correlation of differential pressures. *Int. J. Multiph. Flow* 88, 222–237.

Chapter 5

Summary

Structural health monitoring (SHM) based on machine learning algorithms has been widely used for safe operation and economic benefits. Conventional passive SHM approaches have been influenced by random noise and have a difficulty in detecting locally developed damage. Meanwhile, active approaches for local damage detection are generally operated in offline monitoring (inspection) with prior information about probable locations of damage. In order to overcome limitations of conventional methods, the averaged NCF of diffuse fields has been introduced. Its application to SHM has advantages that it doesn't require active sensing device, where the technique can be applied to monitoring system during operation of structure without disassembly, and it can detect damage of local phenomenon. In this dissertation, we explored a developed experiment to analyze various types of damages with different source generation using the impact hammer. And we studied the effect of diffuse fields by changing the number of sources with random locations. Furthermore, this dissertation proposed a new monitoring approach in the pipeline-riser structure using accelerometers to overcome limitations of conventional measurements such as pressure gauge. The use of accelerometer has advantages: it can be operated in nonintrusive way; it can be transferred after its installation; and the vibration characteristics are considerably different between stable flow and

unstable flow. We applied accelerometers to detect severe slugging with short time signals considering the real-time monitoring.

In chapter 2, machine learning algorithms employed in this dissertation, PCA, SVM, and NN were presented. In chapter 3, we provided the experimental results of damage detectability on the aluminum plate using the cross-correlation of the diffuse field. In chapter 4, early recognition of severe slugging in the pipeline-riser system was investigated based on accelerometer signals.

Contributions of this dissertation are as follows:

- We introduced the averaged NCF of diffuse fields, especially its application to SHM. We performed the developed experiment to analyze two types of damages based on different source generation using the hand-held impact hammer. We can produce more appropriate environmental conditions for marine and offshore structures exposed to wave impact loadings. We also analyzed the effects of diffuse field conditions by changing the number of sources. The experimental results showed that: (1) the passive monitoring based on the averaged NCF of diffuse fields is validated under various environmental conditions; and (2) the incomplete construction of the averaged NCF can be mitigated by the ability of the classifier.
- We proposed a new monitoring approach using vibration signals of accelerometers in the pipeline-riser structure. The use of accelerometer has advantages in its nonintrusive operation and ability of transfer after its installation, which can overcome limitations of the conventional instruments. Experimental results using accelerometers showed that: (1)

flow monitoring can be operated in a nonintrusive fashion; and (2) short time signals such as 2.5 s can recognize the unstable flow, because FIV is significantly different between stable flow and unstable flow. The proposed monitoring approach based on accelerometers improved the possibility of real-time monitoring.

This dissertation can provide some future works for employing the proposed methods to various types of SHM applications, such as blockage monitoring in the pipeline structures. For example, using different feature extraction in the frequency domain, our methods have been detected an early stage of blockage generation in the pipeline from a preliminary experiment. Furthermore, the proposed vibration-based SHM techniques can be applied to real industrial environments using pre-existing accelerometers (e.g., measuring instruments for monitoring vortex induced vibration). We expect that these methods can further improve the established monitoring system by enhancing the accuracy and reliability of the system.

Appendix

A.1. Classification without PCA in damage detection on the plate

The PCA in this study is used for data visualization as well as for classification. Considering the information loss from original data, classification results without using PCA are presented in Fig. A-1 and Table A-1. In case of the hole-punctuated plate, the accuracies become higher than those from two-dimensional data with PCA in Table 3-2. The accuracies of the clay-attached plate are similar to those of two-dimensional data.

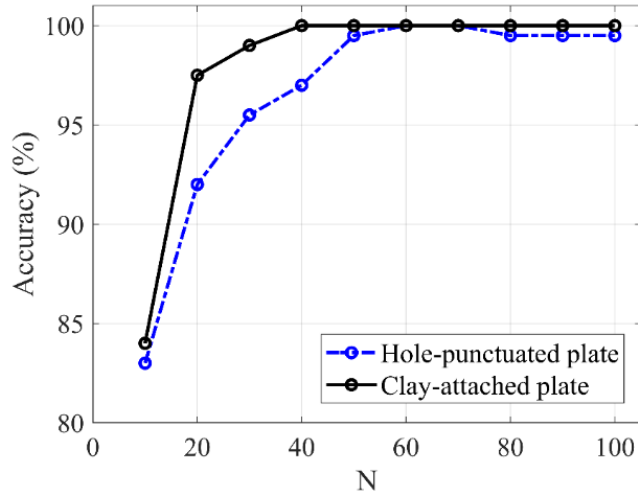


Figure A-1: Averaged accuracy according to the number of sources without using PCA. The blue dashed line presents the hole-punctuated plate, while the black solid line indicates the clay-attached plate.

Table A-1: Binary classification results of the SVM without using PCA.

Hole punctuated plate	N									
	10	20	30	40	50	60	70	80	90	100
Type 1 error (%)	22	13	1	5	1	0	0	1	1	1
Type 2 error (%)	12	3	8	1	0	0	0	0	0	0
Averaged error (%)	17	8	4.5	3	0.5	0	0	0.5	0.5	0.5
Averaged accuracy (%)	83	92	95.5	97	99.5	100	100	99.5	99.5	99.5
Clay attached plate	N									
	10	20	30	40	50	60	70	80	90	100
Type 1 error (%)	15	2	0	0	0	0	0	0	0	0
Type 2 error (%)	17	3	2	0	0	0	0	0	0	0
Averaged error (%)	16	2.5	1	0	0	0	0	0	0	0
Averaged accuracy (%)	84	97.5	99	100	100	100	100	100	100	100

A.2. Optimized parameters in severe slugging detection

In chapter 4, the hyper-parameters of machine learning algorithms are optimized to minimize five-fold cross-validation errors. The optimized parameters for binary classifications are presented in Tables A-2 and A-3. For multiclass classification, the optimized parameters and probabilities of softmax layer for signals 7, 5, and 2.5 s are demonstrated in Tables A-4, A-5, and A-6, respectively.

Table A-2: The optimized parameters of binary classification results in Table 4-3.

Accelerometer	Length of samples (sec)	Kernel	Scale	Box constraint	Polynomial order
1 – 6	7	RBF	1	10	-
	5	Polynomial	1	0.001	4
	2.5	Polynomial	10	100	8
1	7	RBF	1	1000	-
	5	Polynomial	1	1000	4
	2.5	Polynomial	1	100	4
6	7	Polynomial	1	100	5
	5	RBF	1	1000	-
	2.5	Polynomial	1	1000	2

Table A-3: The optimized parameters of binary classification results in Table 4-5.

Accelerometer	Length of samples (sec)	Kernel	Scale	Box constraint	Polynomial order
1 – 6	7	RBF	1	100	-
	5	Polynomial	1	0.1	3
	2.5	Polynomial	1	0.001	4
1	7	Polynomial	1	0.1	9
	5	Polynomial	1	0.1	8
	2.5	Polynomial	1	1	4
6	7	Polynomial	1	10	4
	5	Polynomial	1	100	3
	2.5	Polynomial	1	1000	3

Table A-4: The optimized parameters and probability of multiclass classification results for signals of 7 s in Table 4-6.

Signals of 7 s, Averaged accuracy: 97.16 % Learning rate: 0.01 Layer: [20 20 20]				
	ST	SS1-1	SS1-2	IR
ST	0.9398	0.0225	0.0334	0.0022
SS1-1	0.0227	0.9629	0.0166	0.0036
SS1-2	0.0365	0.0099	0.9486	0.0016
IR	0.001	0.0048	0.0015	0.9927

Table A-5: The optimized parameters and probability of multiclass classification results for signals of 5 s in Table 4-6.

Signals of 5 s, Averaged accuracy: 96.85 % Learning rate: 0.1 Layer: [20 20 20]				
	ST	SS1-1	SS1-2	IR
ST	0.9331	0.0267	0.0405	0.0054
SS1-1	0.0212	0.9546	0.0156	0.0054
SS1-2	0.042	0.0165	0.9384	0.0028
IR	0.0038	0.0022	0.0055	0.9863

Table A-6: The optimized parameters and probability of multiclass classification results for signals of 2.5 s in Table 4-6.

Signals of 2.5 s, Averaged accuracy: 94.11 % Learning rate: 0.001 Layer: [20 10]				
	ST	SS1-1	SS1-2	IR
ST	0.8789	0.0377	0.0759	0.01
SS1-1	0.0457	0.9237	0.0312	0.0089
SS1-2	0.0666	0.0239	0.887	0.0057
IR	0.0088	0.0147	0.0059	0.9754

A.3. Classification with additional features of frequency domain signals

In addition to original feature sets, additional features including mean, RMS, and maximum value of frequency domain signal $|y(f)|$ are investigated (Table A-7). There has no clear difference from classification results using original features in Table 4-3. Further studies of feature selections can be extended which could be useful to identify various flow regimes.

Table A-7: Binary classification results with additional frequency domain features.

Accelerometer	Length of signals (s)	Averaged accuracy (%)	Accuracy for stable flow (%)	Accuracy for severe slugging (%)
1-6	7	99.67	99.89	99.44
	5	97.83	99	96.67
	2.5	97.17	97.56	96.78
1	7	95.67	98.56	92.78
	5	93.72	96	91.44
	2.5	90.5	95.33	85.67
6	7	88.28	96.56	80
	5	86.17	94.33	78
	2.5	83.61	96.56	70.67

초 록

기계 학습을 이용한 진동 기반 구조물 건전성 모니터링 기법의 판과 파이프 구조물에의 응용

정선아

조선해양공학과

서울대학교 대학원

구조물의 건전성 모니터링(structural health monitoring)은 대형 구조물의 안전한 운용과 경제적 효율성을 위해 필수적이다. 구조물의 상태를 모니터링하는 데에는 기계 학습 기반의 통계적 분석이 일반적으로 사용된다. 진동 신호를 기반으로 하는 모니터링 기법들은 주로 구조물의 모드 주파수, 모드 감쇠, 또는 모드 형상과 같은 모드 변수들을 이용하여 구조물의 상태를 분석한다. 그러나 손상은 국소적으로 발생하는 경우가 많고, 특히 주변 진동을 이용하는 감지기법의 경우 국소적으로 발생한 손상이 모드 변수들에 큰 영향을 미치지 못할 수 있다는 한계점이 있다. 최근 주변 진동의 상호 상관 함수에서도 추출되는 신호처리 기법에 대한 연구들이 건전성 모니터링에 유용하다는 것을 보여주었다. 본 논문은 이 기법을 기반으로 확산 장을 이용한 진동 기반의 모니터링 기법을 발전시키고, 알루미늄 판에서 진행된 실험을 통해 이 기법의 유용성을 입증하였다. 두 개의 가속도를 이용하여 두 가지 유형의 손상을 감지하기 위한 실험을 진행하였고, 진동을

발생시키기 위해 충격 해머를 이용하였다. 수신기에서 계측된 진동의 상호 상관 함수들로부터, 손상에 기민하게 반응하는 통계적 특징 벡터를 추출하였다. 서포트 벡터 머신을 이용하여 다양한 진동원의 위치에 의한 환경 조건과 손상 유형에 따라 분류 성능을 분석하였다. 한편, 파이프라인-라이저 구조물의 비정상 유동 모니터링에서는 구조물의 손상과 생산량 저하 등을 유발하는 severe slugging을 빠르게 감지하는 것이 중요하다. 본 논문에서는 기존에 사용되지 않았던 가속도계를 사용하여 severe slugging을 감지하는 새로운 모니터링 기법을 제안하였다. 정상 유동과 비정상 유동 조건에서 진동 신호가 확연하게 다르다는 특징은 빠른 severe slugging의 감지에 유리하게 작용할 수 있다. 수직 라이저에 여섯 개의 가속도계를 설치하여 실험을 진행하였고, 물과 공기의 겹보기 속도 (superficial velocity)를 변화시키면서 서로 다른 환경을 조성하였다. 빠른 신호 처리를 위하여 간단한 통계 파라미터와 선형 예측 계수들로 구성된 특징 벡터를 이용하였다. 이진 분류를 위하여 서포트 벡터 머신을, 다중 클래스 분류를 위하여 뉴럴 네트워크를 사용하였으며, 다양한 길이의 신호와 센서 위치에 따라 분류 성능을 분석하였다. 본 연구에서는 판 구조물의 손상 감지와 파이프라인-라이저 구조물의 비정상 유동 감지를 중점적으로 수행하였으나, 제안하는 기법은 해양 파이프라인의 막힘 감지, 선박 구조물, 빌딩 구조물의 모니터링 등의 다양한 구조물 모니터링 적용에 유용할 것으로 기대된다.

주요어: 구조물 건전성 모니터링, 상호 상관 함수, 주변 진동, severe slugging, 파이프라인-라이저 구조물, 기계 학습

학번: 2015-31036